PHYSICAL REVIEW E **82**, 021606 (2010)

Phase-field study of solidification in three-dimensional channels

Klaus Kassner,[1] Rahma Guérin,[2] Tristan Ducousso,[2] and Jean-Marc Debierre[2]
[1]*Institut für Theoretische Physik, Otto-von-Guericke Universität Magdeburg, Postfach 4120, D-39016 Magdeburg, Germany*
[2]*Institut Matériaux Microélectronique Nanosciences de Provence, Faculté des Sciences et Techniques de Saint-Jérôme,*
Aix-Marseille Université, Case 151, 13397 Marseille Cedex 20, France

(Received 5 May 2010; published 27 August 2010)

Three-dimensional solidification of a pure material with isotropic properties of the solid phase is studied in cylindrical capillaries of various cross sections (circular, hexagonal, and square). As the undercooling is increased, we find, depending on the width of the capillary, a number of different growth modes and dynamical behaviors, including stationary symmetric single fingers, stationary asymmetric fingers, and oscillating double and quadruple fingers. Chaotic states are also observed, some of them in unexpected parameter regions. Our simulations suggest that the bifurcation from symmetric to asymmetric fingers is supercritical. We discuss the nature of the oscillatory states, one of which is chirality breaking, and the origin of the unexpected chaotic finger. Bifurcation diagrams are given comparing three different ratios of capillary length to channel width in the hexagonal channel as well as the three different geometries.

DOI: 10.1103/PhysRevE.82.021606 PACS number(s): 81.10.Aj, 68.70.+w, 81.30.Fb

I. INTRODUCTION

Stationary solidification patterns of a pure undercooled melt in a two-dimensional (2D) channel are known to result from the competition between confinement effects and the interfacial properties of the material, in particular their orientational dependence. Theoretical results [1,2] obtained for low Péclet numbers show that confinement dominates in the weak anisotropy regime. Symmetric fingerlike patterns are then obtained at low undercooling, which become asymmetric at higher undercooling. At high Péclet numbers, interface effects dominate, and the patterns are qualitatively similar to free dendrites or, if anisotropy is small, structures that have been termed seaweed [3]. These theoretical findings were complemented by various numerical studies. The Green's function method [4–6] and finite-difference simulations of the full diffusion problem [7,8] were used to study the one-sided model (assuming the absence of diffusion in the solid). On the other hand, the symmetric two-sided model (assuming equal diffusion coefficients in the two phases) was investigated by analytical methods [1,9] and phase-field calculations [10,11]. Results obtained from 2D phase-field simulations [12] are well understood theoretically [13]. More recently, phase-field simulations have been extended to the one-sided case as well [14].

In three dimensions, no analytical theory is available, the only exception being the free dendrite [15,16] that corresponds to the limit of large channel width in the presence of surface tension anisotropy. Efforts to produce quantitative numerical results have remained very limited so far. This is not so surprising because the starting point of the 2D theory is the Saffman-Taylor finger [17], which has no direct physical equivalent in three dimensions since flows in homogeneous environments are no longer governed by Darcy's law. Instead, a three-dimensional (3D) physical analog of the Saffman-Taylor finger exists for flow through porous media only [18]. In two dimensions, Saffman-Taylor fingers are known to be always symmetric [19] (in the standard setup, i.e., in the absence of asymmetric forcing [20]), and although there is no analogous proof for three-dimensional viscous fingering, only axisymmetric growth has been considered in this system so far [18]. Crystal growth is different in two dimensions already due to nonzero Péclet number effects; hence, asymmetric growth modes exist, even for isotropic surface tension; in three dimensions, asymmetric growth has been found as well [21].

Quantitative 3D simulations are still extremely time consuming. In a pioneering work, Abel *et al.* [21] performed several 3D simulations of a *qualitative* phase-field model (based on sharp-interface asymptotics). This study was focused on isotropic materials and neither the undercooling nor the reduced capillary length (ratio of capillary length to the system width) was varied. A central result was the observation of multiplets (quadruplets and triplets) of asymmetric patterns, depending on the size of the system and the nature of the imposed boundary conditions (mirror vs periodic). Both parameters were discussed to have a direct influence on pattern selection at larger scales. *Quantitative* phase-field simulations of three-dimensional directional solidification structures based on a generalization of Karma and Rappel's thin-interface asymptotics [22] to the case of the one-sided model have been recently performed by Gurevich *et al.* [23].

In the present paper, we use the original quantitative phase-field model for symmetric diffusion [22] (which is more accurate than its one-sided counterpart [24]) to explore similarities and differences of crystal growth in a 3D channel in comparison with the two-dimensional setup. In particular, we investigate the roles of the imposed undercooling, of the reduced capillary length, and the influence of the channel geometry on solidification patterns of isotropic materials. Indeed, an important step when passing from two to three dimensions is to decide how to choose the channel geometry. In two dimensions, the channel is a rectangle, the long edges of which form two parallel lines, with the only characteristic feature being their distance. A straightforward extension to three dimensions would be an elongated cylinder of constant cross section, but there are other possibilities. In the present study, we consider circular, square, and hexagonal channels

1539-3755/2010/82(2)/021606(20)

to explore the specificity of 3D geometric effects of the problem.

The purpose of this paper is twofold. On the one hand, symmetric and asymmetric fingers are expected to exist in three dimensions, too. Their numerical computation will provide quantitative input to a possible extension of selection theory [1,2,9] for crystal growth in a channel or more generally, for the growth of structures beyond the dendrite, to three dimensions. On the other hand, we would like to explore what else there is in three dimensions beyond these simple generalizations of 2D patterns. A much richer variety of dynamical states is anticipated.

The paper is organized as follows. In Sec. II, we give the equations of the underlying moving-boundary continuum model and collect a few simple analytical conclusions on stationary growth following from the basic conservation law. Section III contains the phase-field reformulation of the equations of motion as well as their nondimensionalization and briefly discusses a nonlinear transformation allowing us to simulate larger systems. In Sec. IV, we present simulation results ranging from pattern variety to selected dynamical features, and we summarize our results and some implications in Sec. V. The Appendix describes details of the numerical discretization.

II. BASIC CONSIDERATIONS

It is easy to arrive at a few analytical conclusions highlighting some of the differences between the two- and three-dimensional cases, thus shedding light on a possible influence of the channel shape on growth modes. We consider a model problem that involves a few simplifications, believed not to affect the physics of the system in any essential way. These are the assumptions of equal mass densities and specific heat capacities of the liquid and solid phases, as well as equality of the thermal conductivities in both phases. The first assumption allows us to neglect fluid flow and consider a purely diffusion-controlled situation. Together with the second, it implies that in a two-dimensional steady state the fractional width of the growing finger must be equal to the nondimensional undercooling Δ. The third assumption means that we are dealing with the so-called *symmetric* model of diffusion-limited growth. It can be most easily relaxed and both the one-sided limit [25] as well as all intermediate cases have been considered [26], without qualitative change in the phenomena.

Let us briefly recapitulate the model equations describing the physical problem; the approximating phase-field description will be given in the next section. The bulk field equation, valid in both phases, is the diffusion equation

$$\partial_t u = D\nabla^2 u, \tag{1}$$

where $u=(T-T_M)/(L_H/C_p)$ is the nondimensional temperature, T_M is the melting temperature, and L_H and C_p are the latent heat and heat capacity (at fixed pressure), each referred to a unit volume. D is the thermal diffusion coefficient. Far ahead of the growing structure, a temperature $T_\infty < T_M$ is imposed, leading to $u=-\Delta$ with $\Delta=(T_M-T_\infty)/(L_H/C_p)$, which is the nondimensional undercooling.

The motion of the liquid-solid phase boundary is governed by two equations, one of which is the Stefan condition

$$v_n = -D\mathbf{n}\cdot\nabla u|_l + D\mathbf{n}\cdot\nabla u|_s, \tag{2}$$

with $\mathbf{n}$ being the normal vector on the interface, pointing from the solid into the liquid. v_n is the normal velocity of the interface and the subscripts refer to its liquid and solid sides on which the gradient is to be taken. This equation describes energy conservation at the interface and can be derived from Eq. (1) via integration over a Gaussian pillbox about the two-phase boundary. The second interface equation is the (generalized) Gibbs-Thomson condition, describing capillary (and possibly kinetic) effects on the interface temperature,

$$u_i = -\Delta_\mu[\zeta] - \beta v_n, \tag{3}$$

where $\zeta(x,y,t)$ is the interface position and the subscript i simply means *interface*. We do not have to distinguish between its liquid and solid sides here since u is continuous across the phase boundary. The first term on the right-hand side is given by

$$\Delta_\mu[\zeta] = \frac{C_p T_M}{L_H^2}\left[\frac{1}{R_1}\left(\gamma + \frac{\partial^2\gamma}{\partial\theta_1^2}\right) + \frac{1}{R_2}\left(\gamma + \frac{\partial^2\gamma}{\partial\theta_2^2}\right)\right]. \tag{4}$$

Herein, R_1 and R_2 are the local principal radii of curvature of the interface and θ_1 and θ_2 are the angles between the normal on the interface and two directions determined by the principal curvatures. γ is the surface energy. In general, application of the 3D Gibbs-Thomson condition requires knowledge of the two principal curvatures separately. However, since this study is devoted to the case of isotropic surface tension, the derivatives with respect to the two orientation angles vanish and we obtain the much simpler result

$$u_i = -d_0\kappa - \beta_0 v_n. \tag{5}$$

Here, d_0 and β_0 are the capillary length and kinetic coefficient, respectively. The capillary length is given by $d_0 = \gamma C_p T_M / L_H^2$, and $\kappa = 1/R_1 + 1/R_2$ is the *mean curvature*, taken as positive for a locally convex solid. Often local equilibrium can be assumed, in which case $\beta_0=0$. This is the situation we are interested in here.

Now we will consider some consequences of energy conservation as described by Eq. (1) for steady-state growth. We place ourselves in a frame of reference where the tip of the crystal growing at constant velocity v is at rest. If we choose as the zero point of the internal energy the state of the solid at the melting temperature T_M, a volume element ΔV of liquid far ahead of the tip will have energy $[L_H + C_p(T_\infty - T_M)]\Delta V$. Hence, the energy flux through the cross section A of the channel toward the tip is given by $-vA[L_H + C_p(T_\infty - T_M)] = -vAL_H(1-\Delta)$. Far behind the tip, there will be a two-phase state at thermal equilibrium, with a volume fraction x of the solid and a volume fraction $1-x$ of the liquid. From the Gibbs-Thomson condition (5) we may immediately conclude that in this state the mean curvature of the interface has to be constant as the temperature is constant. If we assume translational invariance of the crystal shaft along the growth direction to hold locally, then one of the principal radii of curvature must be infinite and the cross section of the crystal must be circular (remember that we assume isotropic surface tension). Hence, the equilibrium condition is $u_{\mathrm{eq}} = -d_0/R$, where R is the radius of the cylindrical solid. In dimensional form it reads $T_{\mathrm{eq}} = T_M(1-\gamma/L_H R)$, and the total energy flux through the cross section A is given by

$$\begin{aligned}-vA\{xC_p(T_{\mathrm{eq}}-T_M)+(1-x)[L_H+C_p(T_{\mathrm{eq}}-T_M)]\}\\ =-vAL_H[-xd_0/R+(1-x)(1-d_0/R)].\end{aligned}$$

Equating the two energy fluxes and solving for x, we find

$$x = \Delta - \frac{d_0}{R} \tag{6}$$

to be compared with $x = \Delta$ in the two-dimensional case. In fact, the two-dimensional result is contained in Eq. (6). If we change our channel geometry into two parallel plates, then plate-shaped crystals may grow, meaning that we have solutions that are independent of one of the (appropriately chosen) spatial coordinates, i.e., solutions to the two-dimensional problem. R becomes infinite and we recover the well-known 2D relation.

Equation (6) implies that in the 3D case, we may have a finger solution for *unit* undercooling in a cylindrical channel, besides the traditional family of planar front solutions. Whether this solution has any dynamical implications is a question about its stability which cannot be answered at this point.

Another consequence of Eq. (6) is that the size of the cross section of the growing crystal is not as simply related to the channel width as in the 2D case. We obviously have

$$\pi R^2 = \left(\Delta - \frac{d_0}{R}\right)A, \tag{7}$$

which is a cubic equation for R. For $d_0/R \ll 1$, it is easy to solve this equation approximately.

It is interesting to meditate on a shape effect of 3D channels that has no analog in two dimensions. Essentially, we have argued that the (presumably metastable) equilibrium shape of the crystal shaft in the confined geometry is a circular cylinder [27]. However, such a steady-state solution is impossible for purely geometrical reasons in some geometries, as soon as Δ is large enough that the cross-sectional area required by Eq. (6) would produce a circle, the radius of which exceeds that of the incircle of the channel cross section. Clearly, for a cylindrical channel (with radius R_{cyl}), there is no restriction—a circle satisfying Eq. (7) will fit into the cylinder for all values of $\Delta \leq 1$ because $A = \pi R_{\mathrm{cyl}}^2$. For a square channel with edge a_S and $d_0/a_S \ll 1$, we find that if $\Delta \gtrsim \pi/4 \approx 0.785$, a cylindrical crystal shaft will *not* fit into the channel anymore [the precise relationship is $\Delta \gtrsim \pi/4 + d_0/R$, from which the exact value of $\Delta(d_0, a_S)$ would have to be determined iteratively, as R depends on Δ]. For a regular hexagonal channel, the limiting value of undercooling is $\Delta \gtrsim \pi/2\sqrt{3} \approx 0.907$, a value where steady-state structures are difficult to find—at least symmetric ones. From this point of view, a very interesting case would be a channel with a cross section shaped as an equilateral triangle, because there the critical value is $\Delta = \pi/3\sqrt{3} \approx 0.60$, a value for which we observe steady-state symmetric fingers in sufficiently narrow channels. So far, we have not yet developed a discretization for this geometry.

In realistic physical systems, one will have to consider contact angles in discussing equilibrium as soon as a wall is touched by the crystal. Then the cross section of the equilibrium shape should be composed of several circular arcs having the same radius and touching the walls at an angle determined by Young's equation. Since the radius can be varied to accommodate the angle, this should be satisfiable for arbitrary undercooling. In our simulations, we impose no-flux boundary conditions on the phase field at the channel walls, which means that interfaces of constant phase are locally orthogonal to the wall. While our phase-field model is not designed to ascertain a fixed trijunction angle at a mesoscopic scale, we expect these boundary conditions to approximate a contact angle of 90°.

III. SIMILARITY PHASE-FIELD EQUATIONS

A. Basic model

The problem considered here is solidification of a pure melt in three dimensions. To model this dynamical process, we use the isothermal nonvariational formulation of the thin-interface phase-field model (TIPM) introduced by Karma and Rappel [22] which has been shown to converge to the sharp-interface equations (1), (2), and (5) [or Eq. (3)]. In this model, the temperature and phase fields are both functions of time and space. The phase field φ is a nondimensional variable which takes a value of +1 in the solid phase and −1 in the liquid phase far from the solid-liquid interface and which varies continuously across the interface. The TIPM gives the time evolution of both the temperature and phase fields through two coupled partial differential equations, which take particularly simple forms for an isotropic material:

$$\partial_t u = D\nabla^2 u + \tfrac{1}{2}\partial_t \varphi, \tag{8}$$

$$\tau_0 \partial_t \varphi = F(\varphi, \lambda u) + W_0^2 \nabla^2 \varphi, \tag{9}$$

with

$$F(\varphi, \lambda u) = [\varphi - \lambda u(1-\varphi^2)](1-\varphi^2). \tag{10}$$

It is worth noting that the thermal diffusion coefficient D in the first equation still is a dimensional constant. On the other hand, λ is the nondimensional coefficient coupling the temperature and phase fields. Two more dimensional constants appear in these equations: τ_0 represents a relaxation time while W_0 is the interface width. The asymptotic analysis of the above phase-field equations shows that the dimensional kinetic coefficient and capillary length are related to the model variables and diffusion coefficient through

$$\beta_0 = \frac{a_1 \tau_0}{\lambda W_0} - \frac{a_1 a_2 W_0}{D}, \tag{11}$$

$$d_0 = \frac{a_1}{\lambda} W_0, \tag{12}$$

where $a_1=5\sqrt{2}/8$ and $a_2=47/75$ [22]. In isotropic materials, the solid-liquid interface is expected to be rough, so that the kinetic effects described by β_0 should be negligible. In the present study, we set the kinetic coefficient equal to zero by imposing

$$\lambda = \frac{1}{a_2}\frac{D\tau_0}{W_0^2}. \tag{13}$$

The physical constants d_0 and D are related to the model parameters W_0 and τ_0 by introducing the similarity parameter $\xi=W_0/d_0$, so that

$$W_0 = \xi d_0. \tag{14}$$

From the previous equations, one then obtains $\xi=\lambda/a_1 =(D\tau_0)/W_0^2/(a_1a_2)$, so that

$$\tau_0 = \frac{d_0^2}{D}a_1a_2\xi^3. \tag{15}$$

Essentially, Eq. (13) describes the only nondimensional combination of W_0 and τ_0 occurring; hence, the evolution equations depend on the single similarity parameter ξ. Accordingly, after the time scale τ_0 is set, all the combinations of d_0 and D corresponding to the same value of ξ are modeled by a unique pair of normalized equations. To see this directly, we define the normalized space and time variables

$$\tilde{x} = \frac{x}{W_0}, \quad \tilde{y} = \frac{y}{W_0}, \quad \tilde{t} = \frac{t}{\tau_0}, \tag{16}$$

and the normalized diffusion coefficient

$$\tilde{D} = D\frac{\tau_0}{W_0^2} = a_1a_2\xi. \tag{17}$$

Substituting the regular variables by the normalized ones, we finally arrive at the two similarity equations:

$$\tilde{\partial}_t u = a_1a_2\xi\tilde{\nabla}^2 u + \tfrac{1}{2}\tilde{\partial}_t\varphi, \tag{18}$$

$$\tilde{\partial}_t\varphi = F(\varphi, a_1\xi u) + \tilde{\nabla}^2\varphi. \tag{19}$$

B. Nonlinear transformation

The efficiency of simple nonlinear transformations has been recently demonstrated in the general context of diffuse interface systems [28]. Motivated by the idea to reduce numerical artifacts such as pinning effects, they permit the use of coarser numerical grids to perform reasonably accurate simulations with significantly reduced numerical effort. In the present model, the one-dimensional steady-state solution of the phase-field equation simply reads

$$\varphi_0 = -\tanh(\tilde{x}/\sqrt{2}) \tag{20}$$

in the frame of reference of the interface. Although very appealing by its simplicity, such a profile is not easy to reproduce numerically because meaningful variations of the phase field are restricted to a very narrow spatial interval. According to this observation, the following change of variable is proposed in [28]:

$$\psi = \sqrt{2}\tanh^{-1}(\varphi). \tag{21}$$

This preconditioning of the phase variable transforms the sharp variation of φ across the interface into a quasilinear variation for the new phase variable ψ, which considerably increases the numerical accuracy (of the interface location, for instance). In the vicinity of the phase boundary, $\psi(\mathbf{x},t)$ essentially is a signed distance function indicating both on which side of the interface and how far away from it its argument $\mathbf{x}$ is located. A similar preconditioning could be performed also for the temperature field u (see [28]) but because the temperature field varies more slowly across the interface, linearizing u would be less beneficial.

With the new phase variable, the evolution equations read

$$\tilde{\partial}_t u = a_1a_2\xi\tilde{\nabla}^2 u + \frac{1}{2\sqrt{2}}(1-\varphi^2)\tilde{\partial}_t\psi, \tag{22}$$

$$\tilde{\partial}_t\psi = \sqrt{2}G(a_1\xi u,\varphi) + \tilde{\nabla}^2\psi - \sqrt{2}\varphi|\vec{\tilde{\nabla}}\psi|^2, \tag{23}$$

where

$$G(a_1\xi u,\varphi) = \varphi - a_1\xi u(1-\varphi^2). \tag{24}$$

This change of variable is made for square and hexagonal domains where we use Cartesian coordinates but not for circular domains where polar coordinates are employed. In the following, we constantly work with the nondimensional version of the model, so that we may systematically omit the tildes above the nondimensional variables and differential operators.

IV. SIMULATION

A. General aspects

All simulations are performed with the same similarity parameter $\xi=2.5$. A reasonable convergence of the phase-field results is obtained for this value. The parameters varied in this exploratory study of isotropic systems are the undercooling Δ and the reduced capillary length d_0/L. The channel width L is defined as the diameter of the incircle fit into the channel cross section, which is a quantity with a simple geometric interpretation. Therefore, $L=2R$, a_S, and $\sqrt{3}a_H$ for a circle with radius R, a square with edge length a_S, and a regular hexagon with edge length a_H, respectively. Our introductory considerations would suggest to choose the length scale L equal to the square root of the channel sectional area A, because then crystals growing at the same undercooling in different geometries with the same L would have equilibrated shafts of the same diameter. On the other hand, such a definition would differ by 13% at maximum from the more intuitive one assumed here.

No-flux boundary conditions are used on the lateral boundaries of the channel while at its top the fields are always kept at $\varphi=-1$ and $u=-\Delta$. When preconditioning is used, we impose $\partial_z\psi=-1/W_0$ instead of the condition for φ.

A downward shift of the fields is regularly performed to ensure that the top of the interface remains at roughly constant distance d_f from the far channel boundary in the liquid. That is, every time the distance of the topmost point of the structure from the top of the channel becomes smaller than d_f, we move the whole interior of the system by a fixed small number of mesh spacings toward smaller z values, discarding parts of the tail of the structure in the process and filling up the emptied region near the top of the channel with liquid at temperature $-\Delta$. The distance d_f turns out to be an important characteristic quantity of the finite numerical system, as it determines the minimal velocity of a planar front.

It is well known that in an infinite system Eqs. (1), (2), and (5) admit a planar front similarity solution for $\Delta < 1$, the velocity of which continuously diminishes, being inversely proportional to the square root of time, whereas for unit undercooling, there is a continuous family of constant-velocity planar front solutions. In a channel of finite length, none of the latter solutions survives, but for undercoolings smaller than 1, a constant-velocity solution arises and its velocity is well defined.

To see this, consider the steady-state version of Eq. (1) in a frame of reference moving at velocity v (parallel to the z axis) and assume u to be independent of the coordinates perpendicular to the velocity vector:

$$-vu_z = Du_{zz}. \tag{25}$$

This is a linear first-order equation for u_z, the general solution of which is $u_z = a\exp(-vz/D)$, which can be integrated once more to yield the general solution for u. Using the two boundary conditions (2) and (5) (with $\beta_0 = 0$) together with the requirement that u remains bounded for large negative z, and choosing zero as the z coordinate of the interface, one obtains the well-known

$$u(z) = \begin{cases} 0 & \text{for } z < 0 \\ \exp\left(-\frac{v}{D}z\right) - 1 & \text{for } z \geq 0, \end{cases} \tag{26}$$

with undetermined velocity v. In our finite system, we have the additional boundary condition $u(d_f) = -\Delta$. It is immediately clear that, for $\Delta = 1$, expression (26) is not a solution anymore, because the exponential term cannot become zero; it can become an arbitrarily small positive number at best. The family of solutions (26) is destroyed by the finiteness of the system. On the other hand, for $\Delta \in [0,1)$, the boundary condition is satisfiable and selects the velocity of the planar front:

$$v = \frac{D}{d_f}\ln\frac{1}{1-\Delta}. \tag{27}$$

In a large system, a planar front initialized at homogeneous undercooling will first, after a transient, approach the similarity solution as an intermediate asymptotic state, i.e., its velocity will decrease, but it will not become zero; instead it will approach the limit (27).

Clearly, if finite-size effects can stabilize a planar front at a finite velocity, they might as well stabilize finger solutions at a too high velocity. Therefore, it is essential in the simulations to ascertain a sufficient height of the channel, for example, by increasing this height, once a steady-state finger has been obtained, to make sure that this does not change its velocity anymore. In particular, this is mandatory when the final speed of the finger is not far above the lower-velocity limit (27). We use this procedure in determining the transition from a single symmetric finger toward the planar front, when the undercooling is decreased.

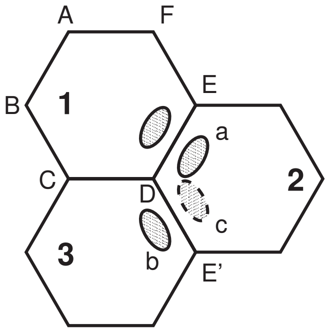

FIG. 1. Hexagonal channel and reflected images.

It may be useful to point out a peculiarity regarding the interpretation of simulation results. Any solution obtained in a quadratic or even merely rectangular channel with reflecting boundary conditions can be interpreted as a possible dynamical state of a laterally infinite periodic array, obtained by repeatedly reflecting the solution at the rectangular boundaries until the plane is filled. The periodicity units of this infinite system will normally be twice the side lengths of the original rectangle (for an exception, see Fig. 5). Of course, this periodic system may be unstable with respect to nonperiodic perturbations or perturbations of a wavelength that exceeds the size of the original rectangle. But a steady-state finger will correspond to an existing solution consisting of an infinite array of fingers—existence is guaranteed, stability is not. Obviously, no such statement can be made for the cylindrical geometry as the basic equations of motion are not invariant with respect to inversion at a circle.

It may be surprising, however, that even solutions in the hexagonal channel cannot be unconditionally extended to the whole plane in general. This is depicted in Fig. 1.

Hexagon 1, with vertices ABCDEF, symbolizes a cross section through the hexagonal channel, the hatched area that of a growing (asymmetric) finger (near its tip). Hexagons 2 and 3 are images, obtained by reflection at DE and CD, respectively, and a and b are the corresponding images of the finger. But a is not obtained by reflecting b along DE′, which rather produces c. Therefore, the pattern cannot be extended to tile the plane. An interpretation of a finger near a wall as part of a pattern with threefold symmetry in a bigger channel (with nonconvex cross section) is only possible if the finger is symmetric with respect to a main diagonal (here, AD) of the original hexagon. For an extension of the pattern to a periodic array, we must have symmetry with respect to all three principal diagonals of the hexagon.

Typical simulations start from an initial condition in which a small solid body with a simple shape is prescribed via initialization of the phase field. We use shapes such as a spherical cap, often a full hemisphere, a cap on top of a cylinder, or—in the case of the hexagonal system—an arrangement of six overlapping caps in order to promote tip splitting. The temperature field is set equal to zero inside the solid and equal to $-\Delta$ outside or it is even set equal to $-\Delta$

TABLE I. Discretization parameters used in the simulations. M is fixed for given d_0/L but N_z changes according to the chosen channel height H.

Cross section	Mesh size	Grid points	
Square	$h_x=h_y=h_z=0.5$	$N_x\times N_y\times N_z$	
		$161\times 161\times 401$	
Circular	$h_\rho=h_z=0.5$	$N_\rho\times N_\varphi\times N_z$	
	$0.5<h_\varphi<1$	$82\times 256\times 483$	
Hexagonal		$[3M(M+1)+1]\times N_z$	
		M	N_z
$d_0=0.005L$: $a=0.7963$, $h=0.6897$		58	697
$d_0=0.007L$: $a=0.7855$, $h=0.6803$		42	505
$d_0=0.010L$: $a=0.7698$, $h=0.6667$		30	721

everywhere. This leads to fast initial growth and a subsequent slowdown of the dynamics.

Arising steady-state structures are normally independent of the initial condition. At low undercoolings, we often use a converged steady finger obtained at higher undercooling as initial condition for the simulation, in order to have faster convergence to the final state.

B. Pattern variety

Details of the discretization procedures for the three geometries considered are given in the Appendix. A few typical sets of numerical grid parameters are gathered in Table I. In the rectangular grid, we denote the mesh spacings by h_x, h_y, and h_z and in the cylinder, where polar coordinates are used predominantly, by h_ρ, h_ϕ, and h_z, with obvious meaning. h_ϕ is variable and constrained between two values; for its precise determination see the Appendix. The discretization of the hexagonal geometry does not have an underlying Cartesian structure, as the hexagonal planes are discretized using a triangular mesh, so we have just two grid parameters: a and h $(=h_z)$.

In the following, structures and dynamics as obtained in the hexagonal channel will be discussed in some detail, whereas we will just comment on their counterparts in the other geometries, where appropriate. We consider three ratios of the capillary length and channel width: $d_0/L=0.01$, $d_0/L=0.007$, and $d_0/L=0.005$, corresponding to situations ranging from strong to intermediate confinement. For each of these, a number of undercoolings Δ are realized, starting at low values for which only the planar front exists and going up to $\Delta=0.8$ or higher. We measure the growth velocity of each pattern and the position of its tip as a function of time as well as other geometric characteristics of the patterns.

Besides the capillary length setting the length unit, the problem involves two natural length scales: the diffusion length

$$\ell=\frac{D}{V}, \tag{28}$$

where V is the tip velocity, and the diameter L of the channel. Both can be used to define a diffusion time. The first of these is given by

$$\tau_d=\frac{\ell}{V}=\frac{\ell^2}{D}, \tag{29}$$

and the second simply by

$$\tau_s=\frac{L^2}{D}. \tag{30}$$

Here, τ_d indicates the time scale on which diffusive transport travels the typical length scale established by the dynamics of the system itself, whereas τ_s describes the time needed for significant diffusive transport across the whole channel. The latter time is a constant for a given system, whereas the former varies with the undercooling. Therefore, for short reference, we will call τ_d the dynamic and τ_s the static diffusion time. The values of the static diffusion times corresponding to the three system sizes considered are $\tau_s=1155.4$ for $L=100d_0$, $\tau_s=2358.1$ for $L\approx 142.8d_0$, and $\tau_s=4621.8$ for $L=200d_0$.

To characterize the solidification dynamics at different undercoolings we use the Péclet number,

$$P=\frac{L}{\ell}=\frac{L}{D}V, \tag{31}$$

as a nondimensional velocity measure that is independent of whether we use the nondimensional or dimensional versions of L, D, and V. We have the simple relationship $\tau_s=P^2\tau_d$. Whenever the system does not approach a steady state, we use the time average of the Péclet number (after transients of the dynamics have decayed) to label the state.

1. Steady-state fingers

In all geometries and for all channel sizes, we find as basic structures, besides the planar front, cylindrically symmetric fingers growing at constant velocity and constant-velocity asymmetric fingers. Symmetric fingers exist at sufficiently low undercoolings, above a threshold that depends on the reduced capillary length d_0/L, and asymmetric fingers appear at higher undercoolings. Details of the bifurcation scenario will be discussed below. Figure 2 visualizes examples of these two kinds. Note that *asymmetric* refers to the loss of *cylindrical* symmetry and that asymmetric fingers still possess a symmetry plane (as will be demonstrated below).

At undercoolings slightly above the symmetry-breaking bifurcation, the resulting asymmetric fingers do not touch the system walls, but as the undercooling becomes larger, their tips move farther off center, until their tail eventually makes contact with a wall. The horizontal cross section of non-touching asymmetric fingers is expected to become circular toward the bottom, too, provided the channel is long enough to permit equilibration. This allows us to check on the quality of our numerics by determining the cross sections for both symmetric and asymmetric fingers and fitting them with circles. Fit parameters are the radius and center coordinates of the circle, which yields an additional means to distinguish between symmetric and asymmetric fingers (originally done by checking whether the tip coordinate is on the center line of the channel or not).

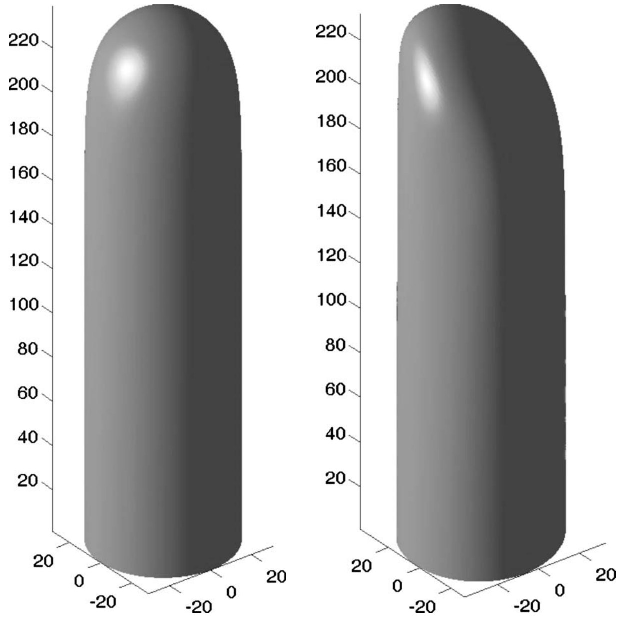

FIG. 2. $d_0/L=0.005$. Left: symmetric finger in hexagonal channel. $\Delta=0.55$. Right: asymmetric finger in hexagonal channel. Its tip distance from the wall is 1.8ℓ. $\Delta=0.65$.

Table II compares the theoretical volume fraction x_{eq} according to Eqs. (6) and (7) with the measured one x_{meas}, obtained by cutting the finger horizontally a few (normally 10) lattice units above the system bottom and calculating the area inside. The aspect ratio, defined as H/L, where H is the system height and L is its diameter, was 12 for the lowest undercooling at $d_0/L=0.005$ and 6 otherwise for this channel size; it varied between 10 and 4 for the system with $d_0/L=0.007$, with lower values corresponding to higher undercoolings, and it was equal to 12 in all the instances of the table given for $d_0/L=0.01$. The system height was larger than 10ℓ in all cases. Moreover, we calculate the equilibrium radius R_{eq} of the finger shaft expected from Eq. (7) and compare it with the fitted radius R_{fit}, giving the relative error $\Delta R \equiv |R_{\mathrm{fit}}-R_{\mathrm{eq}}|$ in percent of the equilibrium radius.

In the largest system ($L=200d_0$), where the radius of the crystal is biggest, the relative error is below a tenth of a percent in all cases. When the size becomes smaller, the ratio of interface thickness and radius increases, and so does the error with respect to the sharp-interface limit, but it stays below half a percent in all simulations.

For the narrowest system, the first asymmetric finger appearing at $\Delta=0.7$ touched the wall already (see Fig. 3). In order to have at least one instance of an asymmetric finger in the table for $d_0/L=0.01$, we measured the radius above the highest point of contact with the wall in this case, where the cross section was still circular.

While visualizations of the three-dimensional structure give an impression of its overall shape, quantitative information about positional aspects and symmetries are more easily gathered from contour plots. Figure 4 shows a sequence of horizontal cuts through the finger from Fig. 3 and a second finger grown for the same parameters but starting from a different initial condition.

TABLE II. Comparison of radii and cross-sectional areas of simulated fingers with analytical prediction. Undercoolings labeled by an asterisk lead to asymmetric fingers (see also Fig. 20).

Δ	x_{eq}	x_{meas}	R_{eq}	R_{fit}	$\Delta R/R_{\mathrm{eq}}$ (%)
			$d_0/L=0.005$		
0.50	0.48634	0.48768	29.29221	29.31990	0.094533
0.55	0.53700	0.53628	30.78004	30.75758	0.072967
0.57	0.55724	0.55658	31.35468	31.33079	0.076197
0.60*	0.58758	0.58697	32.19677	32.17605	0.064345
0.62*	0.60778	0.60737	32.74576	32.74205	0.011325
0.65*	0.63808	0.63758	33.55190	33.56715	0.045446
			$d_0/L=0.007$		
0.54	0.52154	0.51990	21.66684	21.63170	0.162202
0.55	0.53172	0.52982	21.87723	21.84318	0.155606
0.60	0.58253	0.58131	22.89877	22.86496	0.147673
0.62	0.60283	0.60300	23.29427	23.26439	0.128290
0.65*	0.63325	0.63219	23.87473	23.84368	0.130048
0.67*	0.65351	0.65244	24.25368	24.23939	0.058927
			$d_0/L=0.010$		
0.58	0.55442	0.55208	15.63760	15.58945	0.307899
0.60	0.57488	0.56971	15.92352	15.87612	0.297661
0.65	0.62593	0.62204	16.61544	16.57015	0.272568
0.68	0.65649	0.65323	17.01631	16.97350	0.251595
0.69	0.66667	0.66317	17.14774	17.10614	0.242630
0.70*	0.67685	0.67399	17.27812	17.24837	0.172188

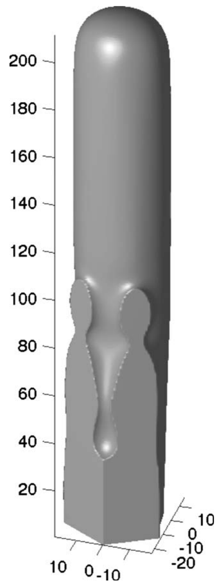

FIG. 3. Steady-state asymmetric finger at $d_0/L=0.01$, $\Delta=0.70$.

These are two different kinds of asymmetric fingers, distinguished by their symmetry properties relative to those of the channel. Both have a single vertical symmetry plane. For the first kind this plane bisects the base hexagon along a main diameter, and for the second it divides the hexagon bisecting two opposite edges. That is, if we now switch to a three-dimensional point of view, the first finger nestles up against an *edge* and the second against a side *face* of the channel. The second kind of finger is extremely rare; almost all of the asymmetric fingers we observe are of the first kind. Nevertheless, the second kind seems to be stable for the parameter set indicated (and stays so on increasing the aspect ratio from 12 to 16).

By reflecting the channel with respect to the two faces adjacent to the edge, to which the first finger clings, one would obtain a triple finger pattern in a bigger channel with a nonconvex cross section, but a pattern that cannot, as discussed above, be periodically continued across the entire base plane. The distance between the finger tip and its reflected image is 4.4 diffusion lengths. Ihle and Müller-Krumbhaar [7] discussed an unbinding transition of a doublon into two asymmetric dendrites and, in the particular example they gave, fingers are considered unbound at a distance of 3.9 diffusion lengths and bound at roughly 1.5 diffusion lengths. Their definition of a diffusion length differs from ours by a factor of 2. Hence, in their terms, the tips of our three-finger pattern are only 2.2 diffusion lengths apart and the pattern might just qualify as a triplon. Moreover, the triplet finger presented in [21] as a prototype of a triplon seems to have a much larger tip distance; a rough estimate from the figure and the given numerical data yields about 6 diffusion lengths (12 in our terminology). Similarly, the second finger in Fig. 4 can be extended, by reflecting it with respect to a side face of the channel, to a double-finger pattern.

A look at the corresponding structures in the square channel may be useful. Figure 5 gives an example.

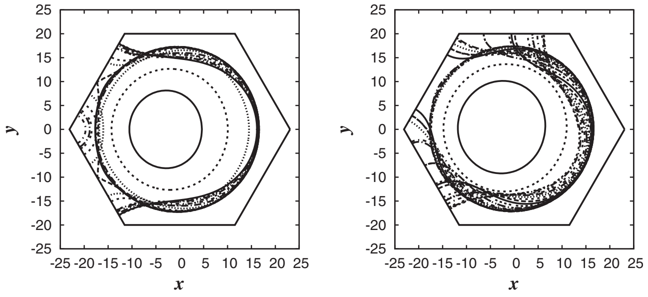

FIG. 4. $d_0/L=0.01$, $\Delta=0.70$. Contour lines for two steady-state finger solutions. Left: finger from Fig. 3, drawing near a channel edge; its tip distance from the wall is 2.2ℓ. Right: finger approaching a channel face; its tip distance from the wall is 2.2ℓ.

Here, we have a four-finger structure that can be periodically extended into all of space along two orthogonal directions. Because the basic pattern is symmetric with respect to two bisectors of the square edges, the periodicity length is not twice the box width but just a single box width. At each corner of the square we have (after inclusion of the reflected images) four fingers growing side by side. These patterns are stable with respect to perturbations that have the basic periodicity but may be unstable to perturbations with a larger period or to aperiodic ones.

To complete this discussion of morphological aspects of steady-state fingers, we may mention that also the conclusions of Sec. II about the behavior of the cross section of a finger touching the system walls are borne out by simulations, assuming a contact angle of 90°. When a finger occupies a sufficient volume fraction of the channel to touch two opposite walls, then the radius of curvature of a circular piece of free boundary between these becomes infinite, i.e., the interface tends to become planar as equilibrium is approached. Such a situation is depicted in Fig. 6, where a cross section of the growing finger has an almost straight free boundary. Clearly, the system is not yet long enough for equilibrium to be fully established. At equilibrium, the temperature near the channel bottom will be equal to the bulk melting temperature without Gibbs-Thomson correction.

At even higher undercooling, an asymmetric finger may touch six walls of the channel (see Fig. 7), requiring the small piece of free boundary remaining to become circular again; more precisely, it will become cylindrical. According to our sign convention for curvature, the radius of curvature must be counted negative in this case, which means that the equilibrium temperature is *above* the bulk melting temperature; the solid is overheated. We have not included a fit of the free boundary piece to a circle in the figure, because the drawn circle would cover the boundary, being indistinguishable from it within the line thickness [29].

In a real system, we would expect nucleation of liquid to take place in the solid once overheating becomes too large. Of course, the phase-field model cannot automatically produce appropriate nucleation events, so the simulation acquires some less realistic features at these high undercoolings.

2. Oscillatory patterns

In the narrowest channel investigated ($L=100d_0$), we found asymmetric steady-state fingers up to the largest un-

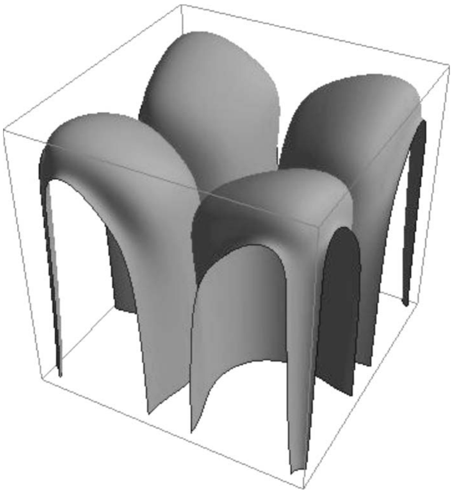

FIG. 5. Stationary solid-liquid interface in a 80.0×80.0 square channel, at undercooling $\Delta=0.75$, $d_0/L=0.005$.

dercoolings considered ($\Delta=0.91$). To see other patterns with comparatively simple dynamics, we had to study wider channels.

In the channels with $L\approx 142.8d_0$ and $L=200d_0$, the asymmetric fingers were followed by oscillatory structures beyond a certain undercooling. These patterns are generic; they appear in the square and cylindrical channels as well, with minor modifications.

The most general aspect of these patterns is that of a double finger. Figure 8 gives two instances and exemplifies the increased level of irregularity of structures at higher undercooling. The subfingers are not equal and there is no symmetry plane anymore. As we shall see, the patterns for $d_0/L=0.007$ can be described as chirality-symmetry breaking, and this is partly visible in the screwlike conformation of the trench between the two fingers in the left panel of the figure. In the larger system ($d_0/L=0.005$), the trench is S shaped, and we shall see that this difference has its correspondence in different dynamics of the two systems.

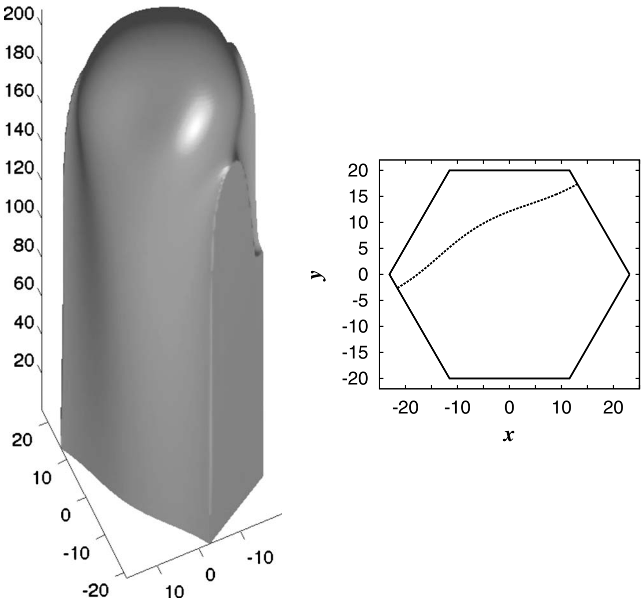

FIG. 6. $d_0/L=0.01$, $\Delta=0.77$. Asymmetric stationary finger. The right picture shows a horizontal section of the finger slightly above the system bottom. The finger touches four walls (occupying more than half the hexagon), so its remaining free boundary is almost straight; the finger tail in the left panel has an almost planar surface. To expose the free interface part of its tail, the finger has been rotated in the left panel.

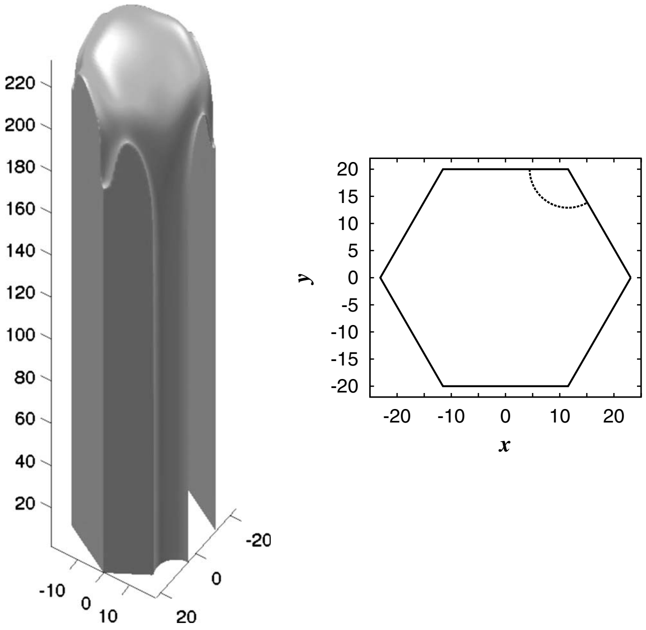

FIG. 7. $d_0/L=0.01$, $\Delta=0.91$. Asymmetric stationary finger. On the right, a horizontal section of the finger slightly above the system bottom is given. The finger touches the wall almost everywhere except at a circular boundary piece. To expose the free interface part of its tail, the finger has been rotated in the left panel.

Oscillations were first detected by measuring the growth velocity of patterns, defined as the velocity of vertical motion of the highest tip of the structure. To obtain a velocity, the tip position of the structure at two successive times has to be determined. This is done by first identifying the lattice position in the base plane above which the interface is highest and then finding the zero (with maximal z value) of the phase field along this line $(x,y)=\text{const}$. By this method, we obtain the tip position with an accuracy that is better than one mesh spacing in the z direction, but only up to a mesh spacing in the lateral directions. The tip velocity is then calculated by dividing the tip z coordinate of two successive time steps by the corresponding time interval. Of course, when there is more than one tip, an exchange of the maximum position will give an inaccurate velocity for the time interval in which the switchover happened. In addition to the so-defined tip velocity we keep track of the lateral tip position at all times.

An example time signal obtained for the tip velocity in an oscillatory system is given in Fig. 9. This run was started from a hemispherical initial condition for the solid and went through different dynamical stages, including a transient steady state and irregular behavior, before becoming periodic after $t=10\,000$ (i.e., after $4.2\tau_s$, in which time the system grew by about 1025 diffusion lengths or 22 times the length

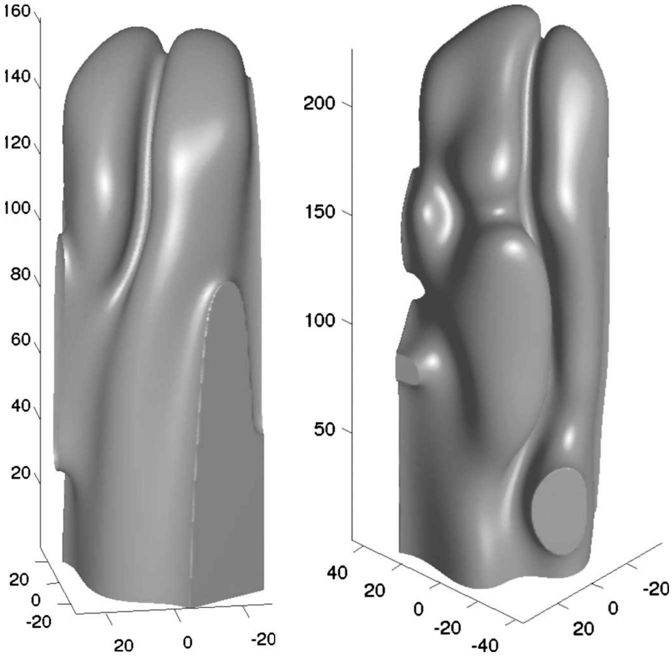

FIG. 8. Oscillating double fingers. Left: $d_0/L=0.007$, $\Delta=0.80$. Right: $d_0/L=0.005$, $\Delta=0.77$.

of the channel). The first maximum in the figure is slightly higher than the maxima of the following periodic stage, so periodicity has not yet fully set in at the beginning of the shown time interval. The oscillations are highly nonlinear and have a complex wave form. We measure frequencies by cutting the signal at appropriately chosen heights and determining the temporal distance between every nth pair of cuts where n is the (even) number of cuts within a period, a number that is normally found by visual inspection. The frequency ν plotted below, in Fig. 12, is the inverse of the period Δt_p.

It is interesting to relate the oscillation period to the different natural time scales of the problem. Given that $\tau_s=2358.1$ for $d_0/L=0.007$, we find the periodicity of the tip velocity in Fig. 9 to be slightly below one third of the static diffusion time. Since the Péclet number for this system is 15.5 (compare Fig. 20 below) the period is long in comparison with the dynamic diffusion time ($\tau_d=9.8$), which renders the rich substructure of an oscillation plausible, but also shows that these oscillations are very sluggish in terms of the intrinsic dynamic time scale. A clearer picture about the nature of the oscillatory state arises from a look at the tip position in the xy plane, which is given in Fig. 10 as a function of time, for the same simulation.

We note that the periodicity of this motion is longer than that of the tip velocity by a factor of 6, and Fig. 11 reveals why. The oscillation is in fact coupled to a rotating motion of the finger, during which the tip moves along a hexagonal path in the xy plane, and since the tip encounters the same conditions along each of the six sides of its path, the periodicity unit of its vertical motion is six times smaller than that of its lateral motion.

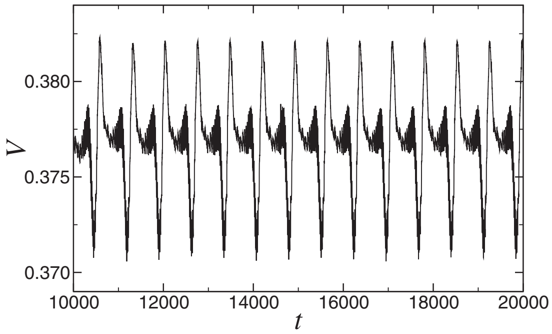

FIG. 9. Oscillations of the vertical component of the tip velocity. $d_0/L=0.007$, $\Delta=0.79$. Period $\Delta t_p=722$. To get rid of high-frequency noise, the signal was smoothed five times with a fourth-order 11-point Savitzky-Golay filter [30].

The same kind of chirality-symmetry breaking dynamics is observed for $\Delta=0.77$ and $\Delta=0.80$. However, in the latter case, another instability threshold has been passed; the six oscillations of the tip velocity during one traversal of the hexagonal tip path become unequal, so that nominally the tip frequency reduces to one sixth, although the sixfold periodicity is still visible in the temporal plot of the oscillations (not shown).

Figure 12 displays the frequencies measured for the observed oscillatory states. Vertical motion refers to the measured tip velocity, while lateral motion refers to the in-plane movement of the tip. Points corresponding to similar dynamical states are connected by lines to guide the eye. The frequency of vertical motion is found to be related to that of the lateral one by a factor of 6, 2, or 1.

The factor of 6, valid for the data points at $\Delta=0.77$ and $\Delta=0.79$ for $d_0/L=0.007$, and the factor of 1 for $\Delta=0.80$ have already been explained. Oscillation periods for lateral motion vary from $\Delta t_p=2994$ to $\Delta t_p=5260$ for these three systems (i.e., from one to two static diffusion times).

The data points at $\Delta=0.78$ for $d_0/L=0.007$ (both at the same position) correspond to a pattern of different appearance and dynamics. Here, we have the rare case of a single oscillating finger. Vertical motion oscillates at a much shorter period ($\Delta t_p=203$) than in the double-finger cases. Laterally, the tip moves back and forth by just one lattice unit in the x direction and stays at the same position along the y axis.

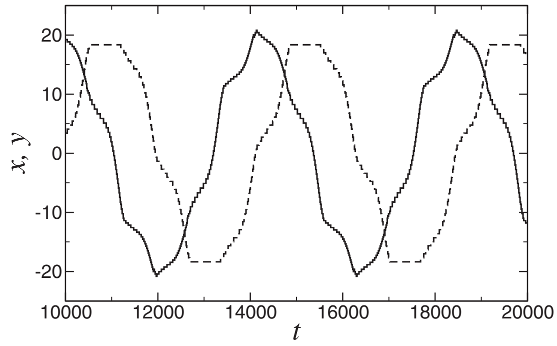

FIG. 10. Oscillations of the x and y components of the (on-lattice) tip position. Solid line: x; dashed line: y. $d_0/L=0.007$, $\Delta=0.79$. Period: $\Delta t_p=4333$.

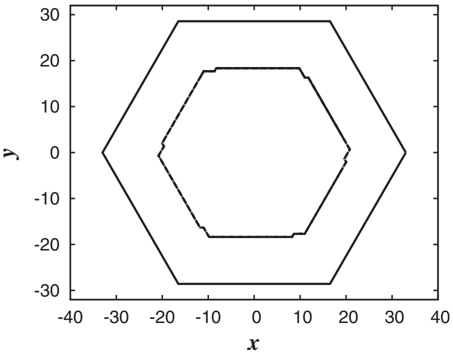

FIG. 11. Path of the tip in the *xy* plane traversed during growth. $d_0/L=0.007$, $\Delta=0.79$. From Fig. 10, we gather that motion is counterclockwise. The tip distance from the wall is 2.5 diffusion lengths.

On the other hand, the data for $\Delta=0.85$ and $d_0/L=0.007$ correspond to a dynamical state that is very similar to the majority of oscillatory states observed for $d_0/L=0.005$ and described by the connected points from $\Delta=0.72$ through $\Delta=0.80$. Here, the factor between the vertical and lateral oscillation frequencies is 2 and this is quickly understood by looking at the in-plane tip trajectory, presented in Fig. 13.

The tip moves back and forth between two next-nearest-neighbor corners of the hexagon. At first sight, one might think that there should be a factor of 4 between the frequencies, but the four pieces of the trajectory are not equivalent. On the way from its leftmost and bottom-most position $x=-16.7$, $y=-29.0$, the tip first moves parallel to the x axis until and a little around the corner of the trajectory (see also Fig. 14). Then both x and y jump, within a single time step, to $x=33.4$ and $y=0$, which is the other extremity of the path. Afterward x and y both decrease slowly until x has decreased below the corner value of $x=16.7$. At approximately $x=4.8$, the x position makes a downward jump to its minimum value of $x=-16.7$, while y remains constant (we are on the bottom edge of the path). These jumps are visible as vertical lines in the time signal of $x(t)$ and $y(t)$, given in Fig. 14. What happens here is obvious: we have two tips that alternately get ahead, and the numerical algorithm always finds the topmost of these. Therefore, only two pieces of the path are equivalent: the way covered by the first tip until the second takes over and the symmetric but opposite way of the second tip, hence only a factor of 2 between the frequencies of vertical and lateral motions.

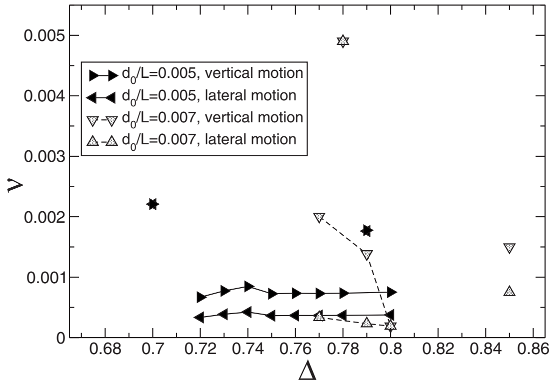

FIG. 12. Frequency $\nu=1/\Delta t_p$ measured for various undercoolings and different oscillatory states. Points for vertical and lateral motions, respectively, correspond to the same simulations. Note that starlike symbols are in fact superpositions of triangles arising when the periodicities of the vertical and the lateral motions are the same.

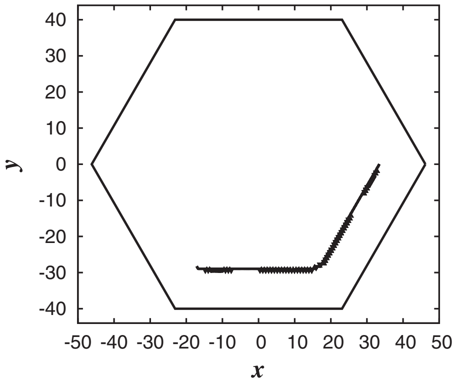

FIG. 13. Path of the tip(s) in the *xy* plane traversed during growth. $d_0/L=0.005$, $\Delta=0.77$. The tip distance from the wall is 2.5 diffusion lengths.

Qualitatively, the appearance of these two major dynamical states can be easily understood. In the smaller channel, there is no room for both tips of the double finger to grow to the same size, so one of them always stays ahead and guides the finger on its merry-go-round tour along the channel wall. In the larger channel, the leading finger tip also seeks its way along the channel wall, but there is now enough room for the trailing finger to catch up. It passes the other finger, blocking it from further continuation of its path and trying to establish motion in the opposite direction, which succeeds only to a certain degree, because the other finger "counterstrikes," and the game starts over again. This kind of dynamics also appears in the smaller channel once the driving force gets large enough (at $\Delta=0.85$).

It should be mentioned that similar oscillatory dynamics are observed in the square channel, although we have not investigated their detailed lateral motion. However, we have done so for a few parameter sets in the cylinder geometry, where a dynamical state exists that is quite similar to what has been described for the hexagonal channel. The tip trajectory travels along the cylinder wall and makes sudden jumps

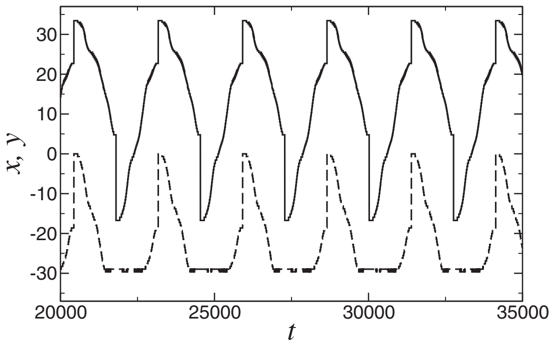

FIG. 14. Oscillations of the x and y components of the (on-lattice) tip position. Solid line: x; dashed line: y. $d_0/L=0.005$, $\Delta=0.77$. Period: $\Delta t_p=2739$.

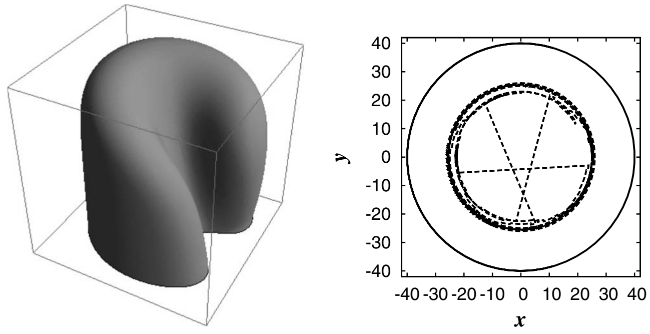

FIG. 15. Left: double finger before tip splitting in the circular channel. $d_0/L=0.005$, $\Delta=0.70$. Right: trajectory of the leading tip (dashed line). The tip distance from the wall (solid line) varies between 2.8 and 3.2 diffusion lengths.

to the opposite side of the cylinder, when the second tip moves ahead. In the case shown in Fig. 15, where Δ is at the lower end of the region of oscillatory double fingers, there is in addition an alternation between a single asymmetric finger and double fingers, appearing via sequences of tip splitting and the falling behind of one finger.

Finally, let us discuss the two outliers at $\Delta=0.7$ and $\Delta=0.79$, $d_0/L=0.005$, for which the vertical and lateral oscillation frequencies agree and are above those of the other undercoolings. Here, the dynamics are entirely different. At $\Delta=0.70$, we have two fingers, not side by side as in Fig. 8 but on opposite sides of the channel (see Fig. 16). They do not move much sideways (there is no motion in the y direction and the x coordinate of the tip oscillates between two neighboring lattice sites), but the vertical velocity oscillates by $\pm 6\%$ about its mean value. The oscillation wave form is simple, far from the complexity of Fig. 9. In the case $\Delta=0.79$, the pattern has two *double* fingers; the velocity oscillation amplitude is below half a percent of the mean value, and two of the four tips alternately get ahead. Note that also at $\Delta=0.8$ the pattern has four fingers, but it is dominated by two of them and the dynamics is largely the same as in the main series of undercoolings between 0.72 and 0.78. It appears that the three patterns having higher oscillation frequencies in Fig. 12 represent situations where the size of the channel suits an almost stationary configuration; they seem to correspond to resonance effects and preferentially appear near the boundary between two types of patterns (see Fig. 20).

An interesting feature of Fig. 12 is that for $d_0/L=0.007$ the frequency of the oscillations decreases with increasing Δ after the first appearance of oscillatory states, whereas in the case $d_0/L=0.005$ it increases first and becomes roughly constant then. While we do not have a clear-cut explanation for this behavior, it demonstrates explicitly that the bifurcation to oscillations must be of Hopf type in the case $d_0/L=0.007$ at least.

3. Complex dynamics

As mentioned before, for $d_0/L=0.010$, we find stationary asymmetric fingers up to the highest undercooling considered ($\Delta=0.91$). This does not mean, however, that all structures observed in this system are steady states. In fact, increasing the undercooling from a symmetric finger configuration to $\Delta=0.75$ (a relatively large jump in undercooling), we obtain a chaotic velocity signal that remains chaotic for long as we care to continue the simulation (well beyond hundred static diffusion times). Decreasing the undercooling of an asymmetric finger from 0.76 to 0.75 produces an ordinary stationary asymmetric finger instead. These two structures coexist, with the average Péclet number of the chaotic finger about 1.5% lower than that of the steady state.

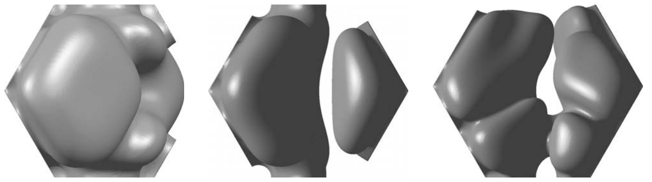

FIG. 16. Top views of the three exceptional oscillatory states. Left: single finger at $d_0/L=0.007$, $\Delta=0.78$. Middle: double finger at $d_0/L=0.005$, $\Delta=0.70$. Right: quadruple finger at $d_0/L=0.005$, $\Delta=0.79$.

More interestingly, at $\Delta=0.74$, *only* a chaotic state seems to exist, whether we take as initial condition a steady-state finger at $\Delta=0.75$ and decrease the undercooling or a steady-state finger at $\Delta=0.73$ and increase it—or choose a different initial condition. The velocity for one of several simulations with these parameters is given in Fig. 17—all of them exhibit the same behavior. Chaotic behavior also appears, not unexpectedly, in the bigger systems, at very high undercooling, but a window of chaotic states inside the interval, where asymmetric stationary fingers dominate, seems to be unique to our smallest system.

A preliminary understanding of this chaotic window may be obtained by comparing the morphologies of steady states appearing below it, at $\Delta=0.73$ and at its upper edge, viz., $\Delta=0.75$, shown in Fig. 18. These fingers have been turned so that the contact line with the walls is seen from a similar view angle. It is tempting to interpret the motion of this line as the steady state of a two-dimensional crystal growth problem. If we assume the contacting wall to be parallel to the xz plane (which is the case for one of the walls in the right panel of Fig. 18), the pertinent "bulk" equation becomes

$$-Vu_z - D(u_{xx}+u_{zz}) = Du_{yy}, \tag{32}$$

where the right-hand side may be interpreted as an imposed inhomogeneity. Because the normal on the contact line lies inside the channel wall, the Stefan condition (2) reduces to its 2D analog. Of course, the Gibbs-Thomson condition (5) retains a contribution from the curvature orthogonal to the wall, so the two-dimensional analogy fails at this point, unless this second radius of curvature is roughly constant. In the limit of small velocities, the bulk equation does not reduce to a Laplace equation as in 2D channel growth, but to a Poisson equation.

The important point to note is that we have just two finger-shaped contact lines at the smaller undercooling and four at the higher one. On the increase of the undercooling,

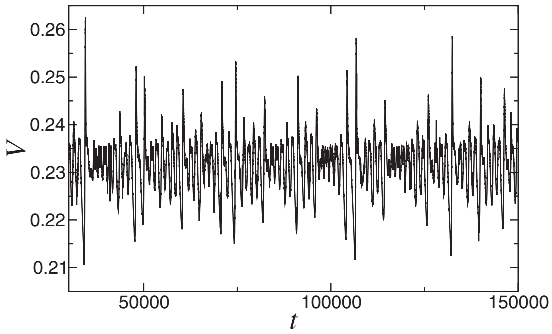

FIG. 17. Typical tip velocity behavior at $d_0/L=0.010$, $\Delta=0.74$ during an extended time interval.

there must be a transition from the first case to the second, and the continuing existence of one symmetry plane (through a channel edge) bisecting the asymmetric finger disallows the appearance of contact line patterns containing an odd number of 2D fingers. In the left panel of Fig. 19, we show the result of this dilemma for the pattern at $\Delta=0.74$.

There is a second 2D finger growing out of the first, but this is not a stable configuration. The other side of the 3D structure is shown in the right panel, and there we see that only one of two 2D fingers has advanced close to the tip, while the other has fallen behind. Moreover, we note that the flat part of the tail of the full three-dimensional finger is roughly orthogonal to its back part near the tip. So the tip of the finger rotates with respect to its tail, similar to the oscillatory screwlike motion of the intermediate-size system discussed in the preceding section, except that in the smaller system the structure never finds a regular state of motion due to the stronger confinement. Hence, chaotic motion inside the existence interval of stationary asymmetric fingers is due to a quantization condition precluding steady-state solutions with an odd number of boundary fingers, at least, as long as the pattern still has a symmetry plane.

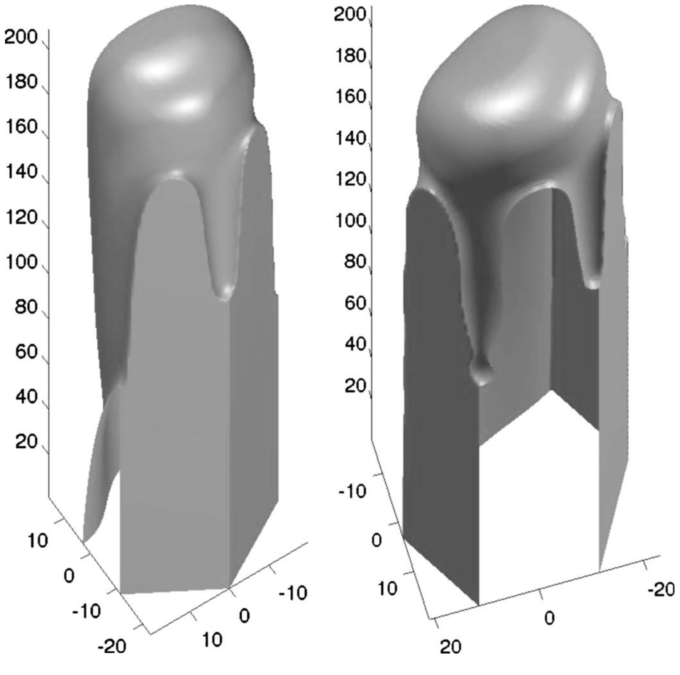

FIG. 18. Stationary fingers at $d_0/L=0.010$. Left: $\Delta=0.73$; right: $\Delta=0.75$. These patterns bracket the chaotic states for Δ in between.

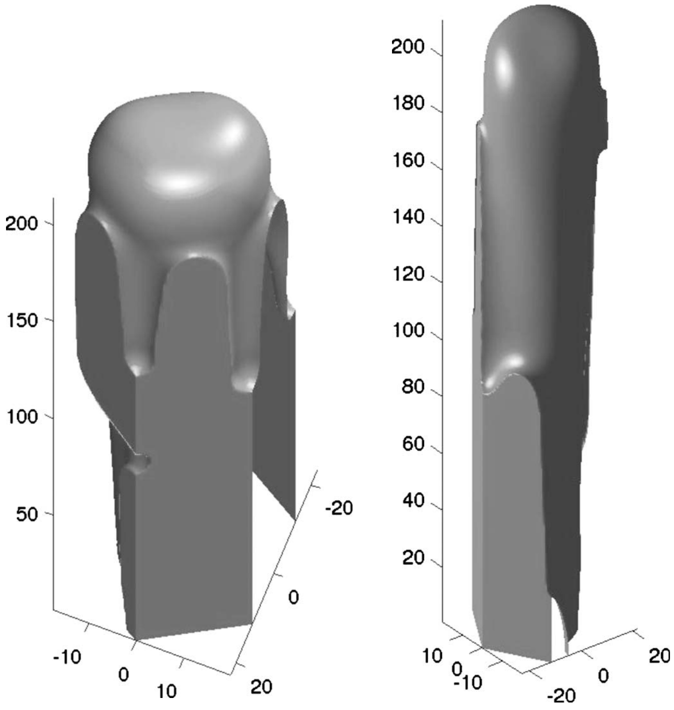

FIG. 19. Chaotic pattern at $d_0/L=0.010$, $\Delta=0.74$. Left: from a similar view angle as the patterns in Fig. 18. Right: view of the same finger from the back of its tip.

For the two larger systems considered, the asymmetric finger suffers its bulk instability leading to oscillatory patterns *before* a third boundary finger could arise besides the two symmetrically arranged ones; hence, there are no chaotic states inside the existence interval of asymmetric steady states.

So far, we have not made an extensive analysis of the chaotic states in the larger systems at undercoolings around and above 0.9. We postpone this to future work.

C. Selected velocities

After having described the major patterns observed, let us now consider the bifurcation structure of the system. To this end, we plot in Fig. 20 the selected Péclet number (or its time average) of a pattern as a function of the imposed undercooling. The scaling of this velocity measure with the system size via Eq. (31) allows us to distinguish confinement-dominated growth (which should lead to a data collapse) from other growth modes. To calculate the Péclet number in Fig. 20, we take an average of the tip velocities over the last 2000 data points, and we verify that taking the last 10 000 points instead does not affect the result beyond the subpercent range. (The spacing between successive data points is $\Delta t=0.5$ or $\Delta t=1$.)

Two transitions that are present in all systems are the bifurcation from a planar front to a symmetric finger and the bifurcation from a symmetric finger to an asymmetric one. In the two bigger systems, this is followed by a transition to

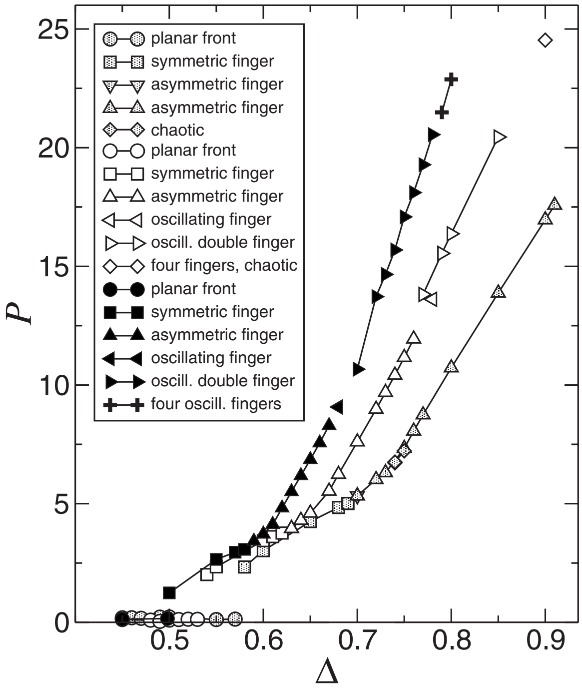

FIG. 20. Bifurcation diagram. Solid black symbols: $d_0/L=0.005$; white symbols: $d_0/L=0.007$; gray symbols: $d_0/L=0.010$.

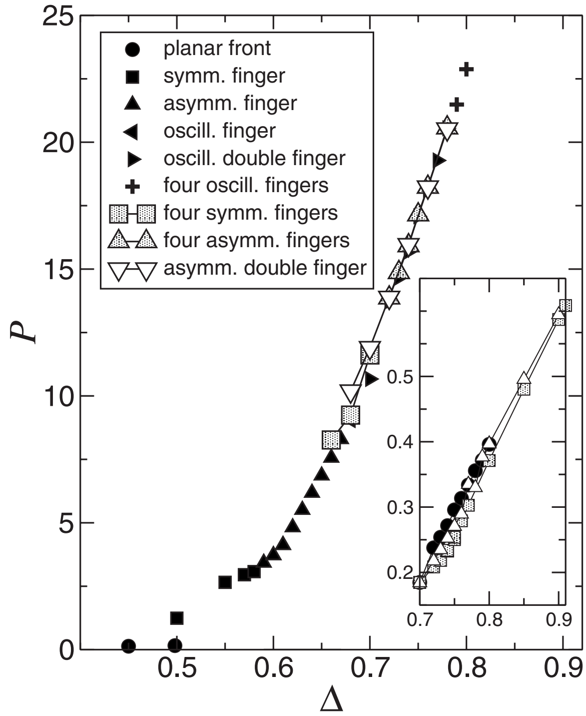

FIG. 21. Comparison of the different geometries; $d_0/L=0.005$. Solid black symbols correspond to the hexagonal channel and appear in Fig. 20 already. Gray symbols: square channel; white symbols: circular channel. New data points have been assigned 50% larger symbols for better distinction. The inset gives the velocity data of Fig. 20 (for $\Delta\geq 0.7$) in unscaled form (i.e., in units of W_0/τ_0).

oscillatory states and transitions to more complex oscillations and chaos.

The points describing symmetric fingers all lie roughly on a straight line. This means that doubling the channel width at a given undercooling will lead to halving the growth velocity of a symmetric finger, provided it exists and is stable in the bigger channel, too. Finger patterns at higher undercooling show no data collapse in this plot, but they do so if the velocity scale for nondimensionalization is taken independent of the system size (e.g., W_0/τ_0; see the inset of Fig. 21). Hence, asymmetric patterns at higher undercoolings grow at a speed that is essentially independent of the channel width and their dynamics is governed by the tip curvature, whereas symmetric fingers grow only *because* of the confinement (they do not exist in an infinite system), and hence slow down when confinement becomes weaker.

To determine the lower existence boundary of symmetric fingers, we take converged patterns as initial conditions for a run with a lower undercooling (increasing the system height as necessary). Initially, the growth rate at the new undercooling decreases, then, if there is a stationary finger solution, the velocity levels out to a new constant value. If there is no steady-state solution anymore, the finger gets thicker and continues to slow down; eventually it hits the system wall. At this point, much latent heat is released and the tip of the structure temporarily reverses its direction, melting back. After that, a planar front grows at a constant velocity, in agreement with Eq. (27). Once a finger starts thickening, it is not really necessary to wait whether it will become a planar front—there seems to be no way for it to avoid this fate.

Because computations at low undercoolings are very time consuming, we have not tried to detect hysteretic behavior by crossing the transition from the planar front to the symmetric finger from below, e.g., starting from a slightly perturbed planar front. In view of the fact that there is no steady-state solution below the symmetric finger in an infinitely long channel, any observable hysteresis might as well be a finite-size effect. In any case, it is to be expected that the weakly nonlinear analysis of planar fronts in free or directional growth [31] carries over to this system without major modifications, which would mean that the bifurcation is supercritical [32,33], because we are dealing with the symmetric model (and, formally, unit segregation coefficient). Clearly, there is a velocity jump on going from the planar front to the symmetric finger, but whether this makes the transition first order or not depends on whether the velocity is the analog of a thermodynamic potential or of a response function (that can jump in second-order transitions).

The larger the system, the lower the transition point Δ_c from a symmetric finger to a planar front. Since we find a stationary finger solution at $L=200d_0$ for $\Delta=0.5$, it seems very unlikely that this undercooling constitutes a lower limit to steady-state growth in the three-dimensional system as it does in the two-dimensional isotropic case. Rather, we expect Δ_c to become even smaller when the channel width is increased further. The cylindrically symmetric version of the equations of motion does not reduce to the two-dimensional stationary diffusion equation [$\nabla^2=\partial_\rho^2+(1/\rho)\partial_\rho+\partial_z^2$, which is not a Laplacian in the ρz plane], so there is no reason to believe that the value $\Delta=1/2$ has any particular significance in the 3D problem. In any case, a limiting width of $2R=0.5L$ in a 2D cut of the system would suggest that the lowest possible undercooling for symmetric fingers with isotropic surface tension in three dimensions is $\Delta=1/4$, if any, rather than 1/2. To check this is beyond our possibilities for the time being.

The bifurcation from the symmetric finger to the asymmetric one happens between $\Delta=0.58$ and $\Delta=0.59$ for $d_0/L=0.005$, between $\Delta=0.62$ and $\Delta=0.63$ for $d_0/L=0.005$, and between $\Delta=0.69$ and $\Delta=0.70$ for $d_0/L=0.010$. As expected, the Péclet number, up to which symmetric fingers exist, decreases with increasing system size; it is $P\approx 4.9$ for $L=100d_0$, $P\approx 3.9$ for $L\approx 142.8d_0$, and $P\approx 3.0$ for $L=200d_0$.

For this transition, we have crossed the bifurcation point both ways and tried to find parameters for which both morphologies coexist. At first sight this appears possible, but running the simulations long enough (i.e., for 25–50 static diffusion times), both the structures obtained by decreasing the undercooling (from an asymmetric solution) and increasing it (from a symmetric solution) systematically become the same. So far, there is just a single case ($\Delta=0.58, d_0/L=0.005$) where we have not yet obtained identity of the two structures initialized differently. We find a well-converged symmetric finger rather fast after increasing the undercooling from $\Delta=0.57$. On the other hand, after decreasing it from $\Delta=0.59$ (using a converged asymmetric finger as initial condition), we find an asymmetric finger, the velocity of which is still decreasing after $t=280\,000$ (≈ 60 static diffusion times), while its tip approaches the channel center in steps (due to requiring it to be on a lattice position). At the time of this writing, it is still two lattice units from the center and the time lags between steps by 1 unit toward the center are increasing, with the last two being 27 600 and 107 500 time units, respectively. We expect this finger to become symmetric after another 200 000−400 000 time steps (corresponding to 1.5–3 months worth of computer time).

In conclusion, although there are definitely long transients, we have seen no hysteresis nor does there seem to be coexistence at steady state. This is unexpected, as the analogous bifurcation from dendrites to doublons is discontinuous [3,7] and the same is true for the transition between a symmetric finger and an asymmetric finger in a two-dimensional channel under variation of the anisotropy of surface tension [7]. Our simulations suggest the transition to be *supercritical* in three dimensions. Since the transients on switchover from one type of finger to the other become extremely long in the vicinity of the bifurcation point, it is easy to mistake a not yet final unstable morphology for metastable. In fact, this slowing down of dynamical changes also speaks in favor of a second-order transition.

There is not necessarily a contradiction here. First, the character of the transition can be different in the cases of isotropic and anisotropic surface tensions; in fact, this is even likely in view of how the nature of a phase transition can be changed by the presence of an external field. Second, while intuitively the transition from dendritic needle crystals to doublon structures must be discontinuous, because it is connected with a topology change, the change from a symmetric to an asymmetric finger in a channel can be easily conceived as a continuous process. Moreover, the first transition cannot happen, unless surface tension anisotropy is present (otherwise, dendrites do not exist), whereas the second is perfectly possible also in the isotropic case. We conclude that the transition is probably continuous for isotropic surface tension and becomes discontinuous, as soon as there is a finite level of anisotropy. Of course, we cannot completely exclude a discontinuous transition—the window of hysteretic behavior could be much smaller than our tested resolution in Δ. On the other hand, the transition to chaos in the system with $L=100d_0$ is discontinuous, at least on the high Δ side, as we have coexistence of chaotic and steady structures.

As to the transitions to oscillatory states, we have not attempted a detailed verification yet concerning their subcritical or supercritical nature due to the presence of normally two different oscillatory states near the beginning of their existence interval. Results for the square and circular channels are similar in the parameter ranges where we compared the three geometries. For reasons of computational cost, we did not investigate very low undercoolings in these systems.

In Fig. 21, we compare data for one size, $L=200d_0$, but three channel shapes. The data for the hexagonal channel are identical to those of Fig. 20.

Note that the Péclet numbers agree for the different geometries, although the patterns do not quite do so. That patterns still remain stationary in the square channel while they are already oscillatory in the hexagonal one is most likely due to the fact that in these simulations the square channel accommodated four fingers, which means that its patterns would fit as a single finger into a channel with $d_0/L=0.01$. A comparison of the patterns with those of the lowermost curve in Fig. 20 shows pretty good agreement: symmetric fingers exist in the square channel up to $\Delta=0.7$, in the hexagonal one up to $\Delta=0.69$, and asymmetric fingers exist at higher undercoolings. That the Péclet numbers agree so well indicates that beyond $\Delta=0.7$, the average velocities in units of W_0/τ_0 are almost the same in all three channels and for all three sizes. Indeed, if the curves in Fig. 20 are rescaled with a factor that is inversely proportional to the linear system size, they exhibit an approximate data collapse for $\Delta>0.7$, as shown in the inset of Fig. 21.

Finally, the patterns in the circular channel given in Fig. 21 are all asymmetric double fingers. For short simulation times, they look as if they were steady states (this is true also in the hexagonal channel), but those, for which the simulation is taken to long enough times, become oscillatory, which agrees with the behavior in a hexagonal channel. We just are not able to extend the simulations to very long times in all cases since this system is suboptimally suited to preconditioning, and hence simulations take much longer times.

V. DISCUSSION AND CONCLUSIONS

A major motivation of this work is to encourage theoretical attempts at an extension of selection theory (on the basis of microscopic solvability or via simpler approaches) to three-dimensional growth in channels. This may be contrasted with the work by Gurevich *et al.* [23] on three-dimensional directional solidification, which aims at a direct comparison with experiments. Unfortunately, similar experiments are lacking for the situation considered here. At least we are not aware of any systematic experimental studies on (isothermal) crystal growth in very thin capillaries.

Due to their more direct link with experiments, the authors of [23] gave the results of their calculations in physical units, whereas we work in a nondimensional (and hence scalable) setting. Nevertheless, it is interesting to relate the nondimensional time unit used here to experimental time scales. The length and time units by which we have rendered equations dimensionless are W_0 and τ_0, respectively. τ_0 is related to physical times via Eq. (15), and the factor $a_1 a_2 \xi^3$ arising there has the fixed value of 8.654 69. The physical time unit is d_0^2/D and it is about one order of magnitude smaller than the numerical one. To get a feeling for typical values, we use material parameters for succinonitrile (SCN) given in [34], $d_0 = 1.3 \times 10^{-2}$ μm, $D = 10^3$ μm^2/s, and obtain $d_0^2/D = 0.169$ μs, which makes our numerical time unit correspond to 1.46 μs. Accordingly, the spacing of our numerical mesh would be 3.25×10^{-2} μm. For our intermediate size system, the channel width would be 1.86 μm, and the periodicity of $\Delta t_p = 722$, presented in Fig. 9, would correspond to 1.06 ms. We have taken the solutal capillary length and diffusivity in this example, whereas our model has symmetric diffusivities, rather describing purely thermal growth. A calculation using the material parameters for SCN given in [35,36] reveals that the thermal capillary length is smaller than the solutal one by almost an order of magnitude, whereas the thermal diffusivity is about two orders of magnitude larger, pushing the time scale down to molecular-dynamics dimensions and turning our capillary into a nanotube. An attempt at modeling these scales with our simple approach would be quite venturous.

On the other hand, the properties of liquid crystal systems may offer much better options for experimental verification of our numerical predictions, because these materials can have large capillary lengths and the diffusivity contrast between the two phases is small, rendering the symmetric model an appropriate description. In the late 1980s and early 1990s, these materials were used as model substances for directional solidification [37] permitting access to dynamical regimes that are difficult to reach or control in ordinary solidification. For example, the workhorse 4-*n*-octylcyanobiphenyl (8CB) has a capillary length of $d_0 = 0.3$ μm and a solute diffusivity of $D = 400$ μm^2/s [37], which translates to a time unit of $\tau_0 = 1.95$ ms, a mesh spacing of 0.75 μm, and in the situation described in Fig. 9, an oscillation period of 1.4 s in a capillary with a diameter of 42.8 μm. Another way to reach large capillary lengths is to make the miscibility gap of alloys small by going to the extreme dilute limit.

Of course, we hope that this work which may be extended easily enough to the study of systems with anisotropy and/or solute diffusion (including asymmetric models) will stimulate experimental investigations to corroborate the basic model assumptions as well as to improve our understanding of the influence of confinement on growth modes. To summarize, we have performed a reasonably extensive exploration of parameter space for crystal growth with isotropic surface tension in three-dimensional hexagonal, square, and circular channels. The anisotropic case is of strong interest, too, but should be considered as the next step.

We find some expected structures—symmetric and asymmetric fingers—and determine their range of existence as a function of undercooling for several system sizes. From our simulations, we see no reason to classify the bifurcation from symmetric to asymmetric fingers as subcritical, but there is some evidence for supercriticality. On the other hand, we do not expect this characteristic to be structurally stable against the introduction of anisotropy.

At undercoolings beyond the range of stability of steady-state single fingers, we find double fingers with oscillatory dynamics to be the predominant species. The nature of the oscillations is strongly confinement dependent—for one system size we find merry-go-round fingers over a certain interval of undercoolings, which are chiral temporally periodic structures. For larger system sizes, the two fingers compete, which renders the time average of the state nonchiral again. In the circular channel, similar periodic states exist, leading to a drift motion of the tip along the wall; the wave form of this oscillation is much more intricate than in the hexagonal system and the phase relation between the x and y coordinates of the tips is more variable. We did not find strong evidence for *triplons* playing a significant role in the dynamics, despite the fact that our hexagonal system was devised to ease their appearance by the removal of all sources of fourfold numerical anisotropy in the planes parallel to the channel base.

A number of reasons may be invoked for this result. Our systems simply may have been too small for stationary triplets to develop inside. Of course, we even see four-finger structures, but they exist in a range of undercoolings, where stationary states are not stable. It should be noted that there was no lack of transient six-finger structures in the initial dynamics of our simulations and that we even had a long-living but nevertheless transient three-finger system, with tips oscillating in the well-known mode with 120° phase shifts [38–40]. Still, it seems that for the spatial dimensions considered, double fingers were preferred over triple ones. This is true for dynamic states at least. Concerning stationary structures, it may be argued that the asymmetric fingers fitting into the 120° wedge of the channel walls form in fact a triplon with their reflected images, and here the observation is that these triplons are much more frequent than their doublonic analogs, consisting of fingers leaning against a single side face of the channel. Since reflected images cannot fall back or advance ahead of their original, the observation of asymmetric fingers in a system with reflecting boundary conditions does not tell us whether the triplon or doublon constructed from them is really stable. Hence, simulations with sufficiently bigger channels (and periodic boundary conditions) should be done to study the stability of triple fingers.

To compare more directly with the approach of Abel *et al.* [21], we first note as an essential difference that in their case the diffusion of the thermal field is slower than that of the phase field, whereas in our case it is faster. As it turns out, the noninteracting parts of the phase-field equations of the two models can be mapped onto each other if the normalized diffusion coefficient $\tilde{D}$ is taken a factor of 3.1 $(=1.5^2 a_1 a_2 \xi)$

smaller in the Abel model. Note that due to Eq. (17), we are not free in the TIPM to choose the ratio of the two diffusion coefficients, once the length and time scales and the similarity parameter ξ are set. To obtain the same ratio as in [21], we would have to choose ξ by a factor of 3.1 smaller; hence, the capillary length would have to become larger by this factor for a given W_0 according to Eq. (14). The Péclet number for the triplon they present is 74.0 at $\Delta = 0.8$, to be contrasted with the maximum value of 22.9 in our biggest channel, with the ratio being 3.2, which suggests approximately equal system sizes L, taking into account the factor between the diffusion constants (and assuming similar velocities in keeping with the results from the inset of Fig. 21). Requiring the time scale of the two simulations to be the same, we may infer from Eq. (15) that—if their kinetic coefficient were zero—indeed the effective capillary length of the system considered by Abel *et al.* would be larger by a factor of ≈ 3.1, meaning that $d_0/L \approx 0.0155$ in their simulation. This would render explicable why they get steady-state structures in spite of the large undercooling. However, it is not unlikely that kinetic effects influence their observed structures, as their model is not devised to ascertain a vanishing kinetic coefficient. Therefore, their simulation might realize a smaller capillary length than estimated here, with the additional stabilization arising from an effectively positive kinetic coefficient.

From the few simulations *with* surface tension anisotropy that we have done so far, we gather that steady-state structures have a larger range of stability in the presence of anisotropy. It is an interesting question for future research to what extent oscillatory states will survive and whether or how their character will change. In general, the question of structural stability of chiral states that we have observed here and which are a genuinely three-dimensional phenomenon may be of some interest (even for applications).

We conclude that as expected there is a much richer structural and dynamical variety in the three-dimensional system than in the two-dimensional one. Some dynamical observations are quite intriguing, such as the emergence of chirality-symmetry breaking states as a realization of oscillations or the appearance of chaos at relatively low undercooling in the smallest system—in which otherwise steady-state growth persists to the highest undercoolings.

ACKNOWLEDGMENTS

We gratefully acknowledge support of this work by PROCOPE Grants No. D/0628184 and No. 14733QC. T.D. benefited from a grant by the Centre National d'Études Spatiales and Région Provence-Alpes-Côte-d'Azur.

APPENDIX: DISCRETIZATION

In the numerical simulations, the phase-field equations have to be discretized for three rather different geometries (square, circle, and hexagon), so that a short comment should be made about the specificities of each case. In all cases, time integration is performed by a first-order Euler algorithm and spatial derivatives are calculated by finite-difference schemes.

For the square geometry, Cartesian coordinates (x,y,z) are used. A seven-point formula is applied to compute the Laplacians and first-order spatial derivatives are obtained by centered differences. This simple scheme is second-order accurate in space. As a consequence, it is expected to generate a small amount of spurious anisotropy.

Using more points in the discretization of differential operators, one can either try to increase the order and, hence, accuracy of the scheme, usually at the price of a less stable code, or to make the error more isotropic. For example, it is possible to write down a second-order accurate 19- or 15-point formula exhibiting an isotropic error at lowest order. That is, anisotropies appear only at fourth order. To derive such a formula, one may start from the ansatz

$$\Delta_d f_{i,j,l} = \frac{1}{a^2}\left\{ \alpha \sum_{\langle i,j,l\rangle} f_{\langle i,j,l\rangle} + \beta \sum_{\langle\langle i,j,l\rangle\rangle} f_{\langle\langle i,j,l\rangle\rangle} + \gamma \sum_{\langle\langle\langle i,j,l\rangle\rangle\rangle} f_{\langle\langle\langle i,j,l\rangle\rangle\rangle} - (6\alpha + 12\beta + 8\gamma) f_{i,j,l} \right\}, \tag{A1}$$

where Δ_d symbolizes the discrete Laplacian, a is the mesh size of the numerical grid, and subscripts within angular brackets mean nearest, next-to-nearest, and third-nearest neighbors of the bracketed lattice site for one, two, and three pairs of brackets, respectively. On the cubic lattice, the first sum comprises six, the second 12, and the third eight terms, so in general, this is a 27-point formula. To obtain appropriate coefficients α, β, and γ, we apply the discrete Laplacian to the discretized plane wave $f_{i,j,l} = e^{\mathrm{i}(k_x ia + k_y ja + k_z la)}$ and require the lowest-order result in $\mathbf{k} = (k_x, k_y, k_z)$ to give the desired continuum limit $-\mathbf{k}^2 f$ and the next order to contain only prefactors proportional to $k^4 = (k_x^2 + k_y^2 + k_z^2)^2$. This leads to the two equations

$$\alpha + 4\beta + 4\gamma = 1, \quad \beta + 2\gamma - \tfrac{1}{6} = 0.$$

Setting $\gamma = 0$, we obtain a 19-point formula with $\alpha = 1/3$, $\beta = 1/6$, involving nearest neighbors and next-to-nearest neighbors. Dropping instead of the third neighbor shell the second one (i.e., taking $\beta = 0$), we have a 15-point formula with $\alpha = 2/3$, $\gamma = 1/12$, which has the advantage of reducing to the two-dimensional "isotropic" Laplacian for functions that do not depend on one of the three coordinates. When using the isotropic Laplacian, we took the 19-point formula, which has the smallest fourth-order error for non-negative γ.

In the nonpreconditioned version (8) and (9) of the model equations, the Laplacian is the only spatial differential operator needed, whereas in the preconditioned version (22) and (23), we also need a discretized gradient. This can be made isotropic up to fourth order in the same spirit, using a ten-point formula for each of the three arising derivatives, in which the two nearest neighbors along the direction of the derivative as well as the four next-to-nearest neighbors surrounding each of those arise, the former with coefficients $\pm 1/6a$ and the latter with coefficients $\pm 1/12a$.

In the case of a circular channel, cylindrical coordinates (ρ, φ, z) are used, for which the Laplacian reads

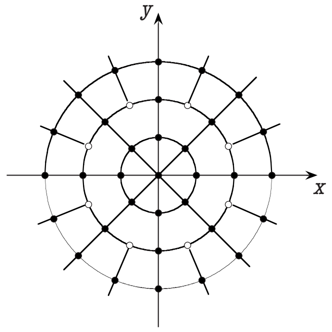

FIG. 22. Grid points used in the cylindrical geometry (black dots). Only the three circles closest to the vertical z axis are shown here. White dots represent intermediate grid points injected on the circle of radius $R_1 = 2h_\rho$: for these points, the fields are obtained by angular interpolation.

$$\nabla^2 = \frac{1}{\rho}\partial_\rho + \partial_{\rho\rho} + \frac{1}{\rho^2}\partial_{\varphi\varphi} + \partial_{zz}. \tag{A2}$$

The spatial discretization is illustrated in Fig. 22. In the (x,y) horizontal plane, one uses concentric circles, of increasing radii, $\rho_i = ih_\rho$ $(i=0,1,\ldots)$. The arclength δs between two neighboring mesh points on the same circle increases with ρ. In order to keep δs smaller than some prescribed value ($\delta s \leq h_\varphi$), the angular resolution is regularly increased at predefined distances R_n $(n=1,2,\ldots)$.

As a consequence, intermediate mesh points must be injected on the circles of radius R_n. For these points, the phase and temperature fields are estimated by interpolation on the whole circle. Thanks to the fact that the total number of points involved is always an integer power of 2, and to angular periodicity, this interpolation can be performed very efficiently and accurately by means of two discrete fast Fourier transforms. The same discretization is repeated at regular mesh distances h_z along the vertical axis z. The Laplacian operator given in Eq. (A2) is not defined for $\rho=0$. It is thus replaced with its Cartesian expression for all the grid points along the z axis.

Our main reason to consider the hexagonal geometry besides the cylindrical and square ones was that triple fingers, conjectured to be the main building blocks of three-dimensional structures arising from diffusion-limited growth with isotropic surface tension [21], remained elusive in the other two geometries. It is quite natural to suspect that in the square geometry this is due to the residual fourfold anisotropy of the discretization, favoring fourfold symmetry over the threefold one. Neither do the basic symmetries of the discretization point pattern in the cylinder seem favorable to the appearance of threefold symmetry. On the other hand, this symmetry would be natural in a hexagonal channel. Nevertheless, we shall see that some care must be taken in the discretization of gradients, in order not to inadvertently reintroduce fourfold anisotropy.

The hexagonal channel is divided into a stack of equidistant planes with spacing h, each of which is discretized using the same triangular grid with lattice constant a. By choosing two integer subscripts to enumerate them, the grid points are effectively mapped to a rectangular scheme (see Fig. 23).

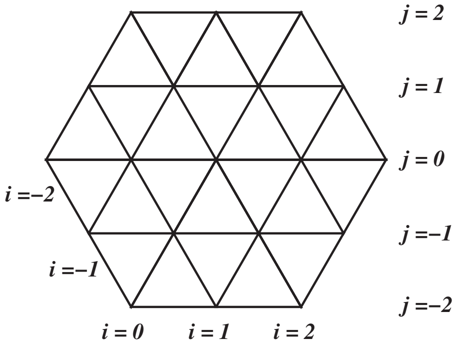

FIG. 23. Numbering of grid points in the hexagonal geometry.

But a rectangular matrix holding the field values of one lattice plane would only be filled to three quarters. Therefore, in order not to waste memory in the numerical computations, we mapped the pair (i,j) of subscripts in a lattice plane to a one-dimensional index $r(i,j)$, so that all field values were effectively stored in two-dimensional arrays, for example, $u(x,y,z) = u_{r,l}$, where l is the number of the lattice plane, and $x(i,j) = (i+j/2)a$, $y(i,j) = (\sqrt{3}/2)ja$, and $z(c) = lh$. The mappings $(i,j) \to r(i,j)$ and $r \to (i(r),j(r))$ were kept in look-up tables. Figure 24 visualizes the order, in which the label r numbers lattice sites: starting at $r=1$ in the center, the label increases in steps of 1 along the indicated spiral. The spiral arrangement has the advantage that the system boundary corresponds to contiguous r values. We realize periodic or no-flux boundary conditions by adding a layer of lattice sites outside the system walls and providing field values there; this is facilitated by having a system boundary that corresponds to a contiguous r sequence.

In discretizing the Laplacian on the numerical grid described, we find that the standard formula

$$\Delta_d f_{i,j,l} = \frac{2}{3a^2}\left\{\sum_{\langle i,j\rangle} f_{\langle i,j\rangle,l} - 6f_{i,j,l}\right\} + \frac{1}{h^2}(f_{i,j,l+1} + f_{i,j,l-1} - 2f_{i,j,l}), \tag{A3}$$

where $\langle i,j\rangle$ denotes in-plane nearest neighbors of (i,j), has already an error that is isotropic in the hexagonal planes, but

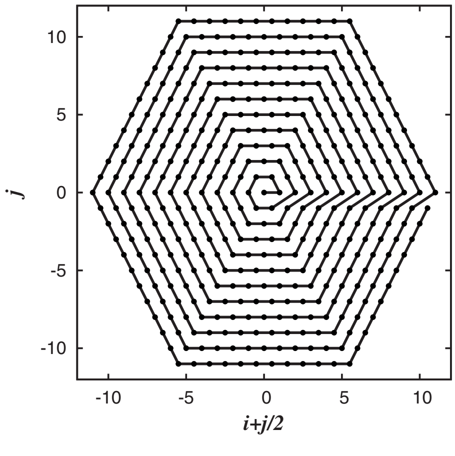

FIG. 24. The mapping of grid point labels i,j to a one-dimensional label. Details are given in the text.

even taking into account the 12 next-to-nearest neighbors, it cannot be made isotropic in the out-of-plane directions, unless $h=\sqrt{3}a/2$. That is, for other values of h a 21-point formula would be insufficient to make the error term isotropic at lowest order. Therefore, we chose this value for h, but for efficiency reasons we stuck to the nine-point formula (A3). For simulations of the nonpreconditioned model we need not go further. However, since the preconditioned model enables simulations, at the same accuracy, with lattice spacings that exceed those of the nonpreconditioned one by about a factor of 2, which corresponds to a gain of a factor of 32 in computing time in 3D systems, the effort of discretizing gradients with isotropic in-plane error is worthwhile.

The point is that if we discretize ∂_x and ∂_y by simple central differences, we will have to treat these two directions differently, as x corresponds to a lattice direction but y does not. We have tried this naive discretization and find that it may lead to the growth of fourfold finger structures from a spherical cap initial condition. A better approach is the following: if we denote by ∂_{a_n} (with $n=1,\ldots,3$) the directional derivatives in the three symmetric lattice directions $\mathbf{a}_1=\mathbf{e}_x$, $\mathbf{a}_{2/3}=-\mathbf{e}_x/2\pm\sqrt{3}\mathbf{e}_y$, then it is easy to verify that any scalar product of gradients (and they appear only in scalar products in the equations) may be written as follows:

$$\nabla A\cdot\nabla B=\frac{2}{3}\sum_{n=1}^{3}\partial_{a_n}A\,\partial_{a_n}B+\partial_z A\,\partial_z B. \tag{A4}$$

Using central differences for all of the appearing derivatives [e.g., $\partial_{a_2}A\to(A_{i-1,j+1,l}-A_{i+1,j-1,l})/2a$], we obtain formulas that know nothing about an x or y direction and indeed have isotropic lowest-order error in the xy plane. Moreover, growing an unstable crystal finger starting from a spherical cap, we now obtain tip splitting sequences leading to six or even 12 fingers, showing that the fourfold anisotropy has been successfully eliminated. (Higher-order errors have sixfold anisotropy.)

---

[1] E. A. Brener, M. B. Geĭlikman, and D. Temkin, Sov. Phys. JETP **67**, 1002 (1988).

[2] E. A. Brener and V. I. Mel'nikov, Adv. Phys. **40**, 53 (1991).

[3] E. A. Brener, H. Müller-Krumbhaar, and D. Temkin, Phys. Rev. E **54**, 2714 (1996).

[4] D. A. Kessler, J. Koplik, and H. Levine, Phys. Rev. A **34**, 4980 (1986).

[5] E. Brener, H. Müller-Krumbhaar, Y. Saito, and D. Temkin, Phys. Rev. E **47**, 1151 (1993).

[6] R. Kupferman, D. A. Kessler, and E. Ben-Jacob, Physica A **213**, 451 (1995).

[7] T. Ihle and H. Müller-Krumbhaar, Phys. Rev. E **49**, 2972 (1994).

[8] H. Emmerich, D. Schleussner, T. Ihle, and K. Kassner, J. Phys.: Condens. Matter **11**, 8981 (1999).

[9] M. Ben Amar and E. Brener, Phys. Rev. Lett. **75**, 561 (1995).

[10] F. Marinozzi, M. Conti, and U. M. Marconi, Phys. Rev. E **53**, 5039 (1996).

[11] R. Guérin, J.-M. Debierre, and K. Kassner, Phys. Rev. E **71**, 011603 (2005).

[12] M. Sabouri-Ghomi, N. Provatas, and M. Grant, Phys. Rev. Lett. **86**, 5084 (2001).

[13] E. A. Brener and D. A. Kessler, Phys. Rev. Lett. **88**, 149601 (2002).

[14] T. Ducousso, R. Guérin, and J.-M. Debierre, Eur. Phys. J. B **70**, 363 (2009).

[15] M. Ben Amar and E. Brener, Phys. Rev. Lett. **71**, 589 (1993).

[16] E. Brener, Phys. Rev. Lett. **71**, 3653 (1993).

[17] P. G. Saffman and G. Taylor, Proc. R. Soc. London, Ser. A **245**, 312 (1958).

[18] H. Levine and Y. Tu, Phys. Rev. A **45**, 1044 (1992).

[19] R. Combescot and T. Dombre, Phys. Rev. A **38**, 2573 (1988).

[20] E. Brener, H. Levine, and Y. Tu, Phys. Fluids A **3**, 529 (1991).

[21] T. Abel, E. Brener, and H. Müller-Krumbhaar, Phys. Rev. E **55**, 7789 (1997).

[22] A. Karma and W. J. Rappel, Phys. Rev. E **53**, R3017 (1996); **57**, 4323 (1998).

[23] S. Gurevich, A. Karma, M. Plapp, and R. Trivedi, Phys. Rev. E **81**, 011603 (2010).

[24] T. Ducousso, Ph.D. thesis, Université d'Aix-Marseille III, 2009.

[25] C. Misbah, J. Phys. (France) **48**, 1265 (1987).

[26] A. Barbieri and J. S. Langer, Phys. Rev. A **39**, 5314 (1989).

[27] Since for isotropic surface tension the equilibrium shape of a crystal not touching any wall is a sphere, one might wonder whether the cylindrical shaft would not have to decay into a sequence of spheres after sufficiently long time, approaching the true equilibrium via a Rayleigh-plateau type of instability. We did not observe any tendency toward such a change of state. Of course, we may be talking really long times and really large system heights here, well beyond numerical accessibility. On the other hand, it can be easily verified that, for undercoolings $\Delta>0.25$, the radius R_s of the resulting spheres would have to be smaller than twice the radius R of the cylinder, meaning that the equilibrium coexistence temperature $-2d_0/R_s$ would be smaller than that of the cylindrical shaft ($-d_0/R$). It is difficult to see how this new state could arise, via an infinitesimal local perturbation, from the homogeneous-temperature equilibrium state involving a cylindrical shaft. The transition would require the establishment of new temperature gradients in an already equilibrated system. Moreover, the temperature would have to go through a maximum in the approach to equilibrium, and this in an adiabatic system. For these reasons, we presume the cylindrical state to be metastable at least.

[28] K. Glasner, J. Comput. Phys. **174**, 695 (2001).

[29] The finger in Fig. 7 has a symmetry plane bisecting the hexagonal base face from its lower left to its upper right corner (in the right panel), meaning that there is no difference between the two vertical system boundaries adjoining the circular/cylindrical segment of the free boundary. That one of the pieces where the finger touches the wall appears massive, whereas the other is open (as it should), is due to the visual-

ization software (MATLAB), working only with rectangular arrays. Fields defined on a stack of planes with a triangular grid had to be transferred to a rectangular domain, with the consequence that faces of the hexagonal prism not parallel to the *xz* plane are not recognized as system boundaries anymore; hence, a piece of interface has to be put on them for plotting purposes. There is no such problem in the square channel.

[30] W. H. Press, S. A. Teukolsky, W. T. Vetterling, and B. P. Flannery, *Numerical Recipes: The Art of Scientific Computing* (Cambridge University Press, Cambridge, England, 2007), Sec. 14.9.

[31] D. J. Wollkind and L. A. Segel, Philos. Trans. R. Soc. London, Ser. A **268**, 351 (1970).

[32] B. Caroli, C. Caroli, and B. Roulet, in *Solids Far from Equilibrium*, edited by C. Godrèche (Cambridge University Press, Cambridge, England, 1992), p. 155.

[33] J. S. Langer and L. A. Turski, Acta Metall. **25**, 1113 (1977).

[34] B. Echebarria, R. Folch, A. Karma, and M. Plapp, Phys. Rev. E **70**, 061604 (2004).

[35] W. Losert, B. Q. Shi, and H. Z. Cummins, Proc. Natl. Acad. Sci. U.S.A. **95**, 431 (1998).

[36] M. Muschol, D. Liu, and H. Z. Cummins, Phys. Rev. A **46**, 1038 (1992).

[37] A. J. Simon, J. Bechhoefer, and A. Libchaber, Phys. Rev. Lett. **61**, 2574 (1988).

[38] I. Daumont, K. Kassner, C. Misbah, and A. Valance, Phys. Rev. E **55**, 6902 (1997).

[39] K. Kassner, J.-M. Debierre, B. Billia, N. Noël, and H. Jamgotchian, Phys. Rev. E **57**, 2849 (1998).

[40] M. Plapp and M. Dejmek, EPL **65**, 276 (2004).